PRELIMINARY DESIGN OF THE LAICE-F MISSION
TO STUDY ATMOSPHERIC GRAVITY WAVES

BY

ISABEL ANDERSON

THESIS

Submitted in partial fulfillment of the requirements
for the degree of Master of Science in Aerospace Engineering
in the Graduate College of the
University of Illinois Urbana-Champaign, 2023

Urbana, Illinois

Advisor:
      Clinical Associate Professor Michael Lembeck

ABSTRACT

The Lower Atmosphere/Ionosphere Coupling Experiment – Follow on (LAICE-F) is a 6U CubeSat mission to study atmospheric gravity waves in the ionosphere through in-situ measurements and remote sensing. This mission is a partnership between Virginia Polytechnic Institute and State University (VT) and the University of Illinois at Urbana Champaign (UIUC). The original LAICE was funded by the NSF and the instruments are being repurposed and flown on the new LAICE-F mission. The UIUC payload, a 7-channel photometer, provides remote sensing of the airglow brightness variations in the lower atmosphere. The VT suite has three payloads all taking in-situ measurements. The retarding potential analyzer (RPA) measures ion density and temperature measurements. The LAICE Ionization gauge Neutral Sensor (LINAS) and Space Neutral Pressure Instrument (SNeuPI) both measure neutral density. The design of LINAS is flight proven and it will be used to verify SNeuPI, a technology demonstration that provides neutral density measurements at a lower mass and power. The mission objectives of LAICE-F are to measure airglow brightness in the lower F-region heights of the atmosphere, to take in-situ measurements of ion and neutral density, and to correlate these measurements and create maps of active gravity wave regions.

ACKNOWLEDGMENTS

To my parents, for your lifelong love and support

TABLE OF CONTENTS

LIST OF FIGURES

LIST OF TABLES

CHAPTER ONE: INTRODUCTION

In 2012, Virginia Polytechnic Institute and State University (VT) and the University of Illinois at Urbana Champaign (UIUC) were awarded funding from the National Science Foundation (NSF) for the original *Lower Atmosphere/Ionosphere Coupling Experiment* (LAICE) 6U CubeSat (Figure 1) to study atmospheric gravity waves in low Earth orbit (LEO). Originally scheduled to launch in 2016 and deploy off the International Space Station (ISS), LAICE included three instruments from VT, with Dr. Gregory Earle as the principal investigator (PI). The UIUC payload is a seven-channel photometer, with Dr. Garry Swenson as the PI leading the research and design.
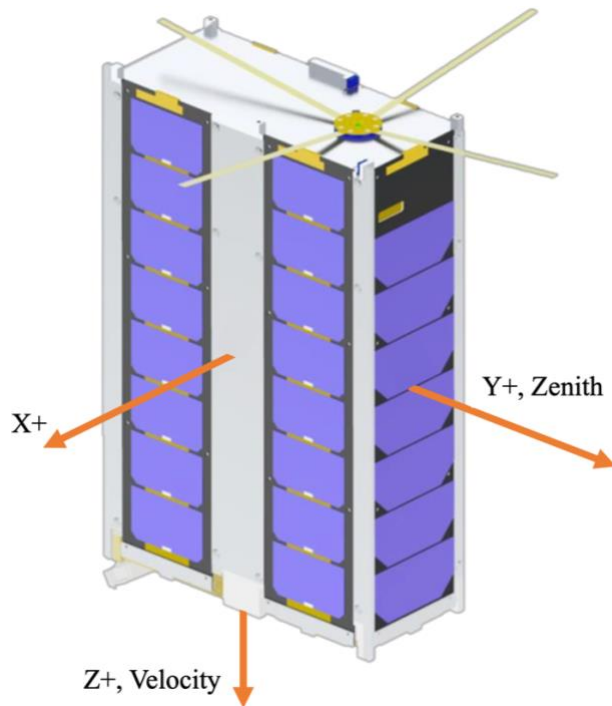
Figure 1: Original LAICE configuration

LAICE was intended to investigate energy and momentum transferred by gravity waves in the low atmosphere into the upper mesosphere and lower thermosphere. The coupling

processes between these atmospheric regions is not well understood and this experiment aims to provide insight using in-situ and remote sensing instruments.

Wind over mountainous regions and weather phenomena on earth, such as hurricanes, tornadoes, and thunderstorms, produce gravity waves that travel up into the atmosphere, carrying energy and momentum into the D, E, and F regions of the ionosphere, seen in Figure 2, which are located in the mesosphere and thermosphere [1]. In the F region where LAICE would orbit, the in-situ VT instruments would measure the variation in ion and neutral densities gravity waves create. In the D and E layer, LAICE would utilize remote sensing with the UIUC payload to measure airglow brightness to determine wave parameters.

LAICE would provide in-situ measurements of ion density and temperature via the retarding potential analyzer (RPA), along with neutral density measurements from the Space Neutral Pressure Instrument (SNeuPI), a prototype instrument that will be validated by the LAICE Ionization gauge Neutral Atmosphere Sensor (LINAS). Remote sensing is provided by the seven-channel photometer which would observe gravity wave induced perturbations in the airglow.
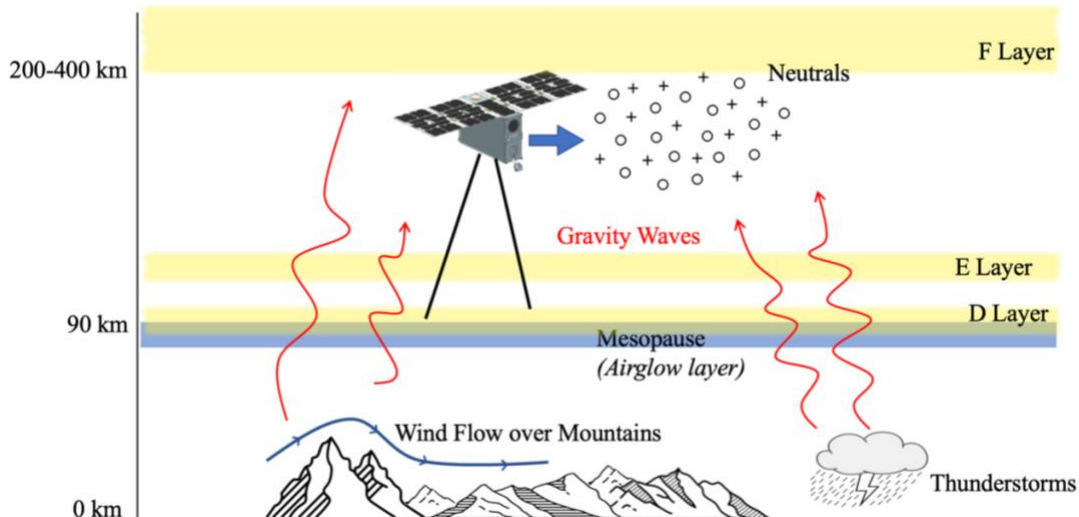
Figure 2: Gravity waves generated by airflow over mountains and weather

The initial program went through a definition and design phase culminating in a Critical Design Review (CDR) in late 2014. At that point in the program, the Federal Communications Commission (FCC) withheld licensing for LAICE due to concerns regarding its potential for endangering the general public upon re-entry based on a required Orbital Debris Assessment Report (ODAR). The FCC is responsible for assessing liability for objects launched from US soil. Part of the payload included a stainless-steel canister that the FCC judged to have a small probability of survival. The hardware for LAICE was then stored for the next six years, until NASA was able to resolve the ODAR licensing issue in 2020 and provided funding to refurbish LAICE. Shortly thereafter, the hardware was removed from storage and additional mission analysis was performed and acceptance testing began on the hardware.

The analysis, performed by a group of students unaffiliated with the original LAICE design, produced several findings. LAICE was configured with body-mounted solar panels, as seen in Figure 1, which allowed for continuous power generation as the LAICE's orbit experienced nodal regression but due to the limited area available, the power produced would have been insufficient to operate the payloads through all mission phases. During some parts of the year, the power generating area was limited to the smallest solar panel (Y+ panel) and would produce an average of 3.5 W per orbit. During these periods, LAICE would be limited to only essential operations, with all science and communications turned off, until the battery, made up of two Lithium ion cells, could be charged above 50%.

Even in its standard operational mode, LAICE had severe power limitations that only permitted science operations for limited durations during eclipse, with LINAS operating on a 10% duty cycle (i.e., available for only the first three minutes of each eclipse period). Acceptance testing of the original LAICE hardware was performed in the Laboratory for

Advanced Space Sciences at Illinois (LASSI). LASSI has supported this mission since the project came back online in January 2021 and has been partnering with NanoAvionics, an aerospace component company located in southern Illinois, for the development of high reliability CubeSats. LASSI supports students, faculty, and other customers utilizing small satellite resources designed, developed, and tested at the University of Illinois at Urbana-Champaign.

In support of the aforementioned analysis, additional component testing, outlined in Chapter Two, found the original LAICE hardware was not flight worthy. As a result of these findings, a new mission, repurposing the LAICE instrumentation was defined as the ***Lower Atmosphere/Ionosphere Coupling Experiment – Follow on*** (LAICE-F). LAICE-F is also a 6U CubeSat mission in LEO. It incorporates a set of deployable solar arrays to provide sufficient power throughout the orbital year to maximize instrument availability (Figure 3). This thesis details the requirements formulation and analysis performed to assess mission feasibility.
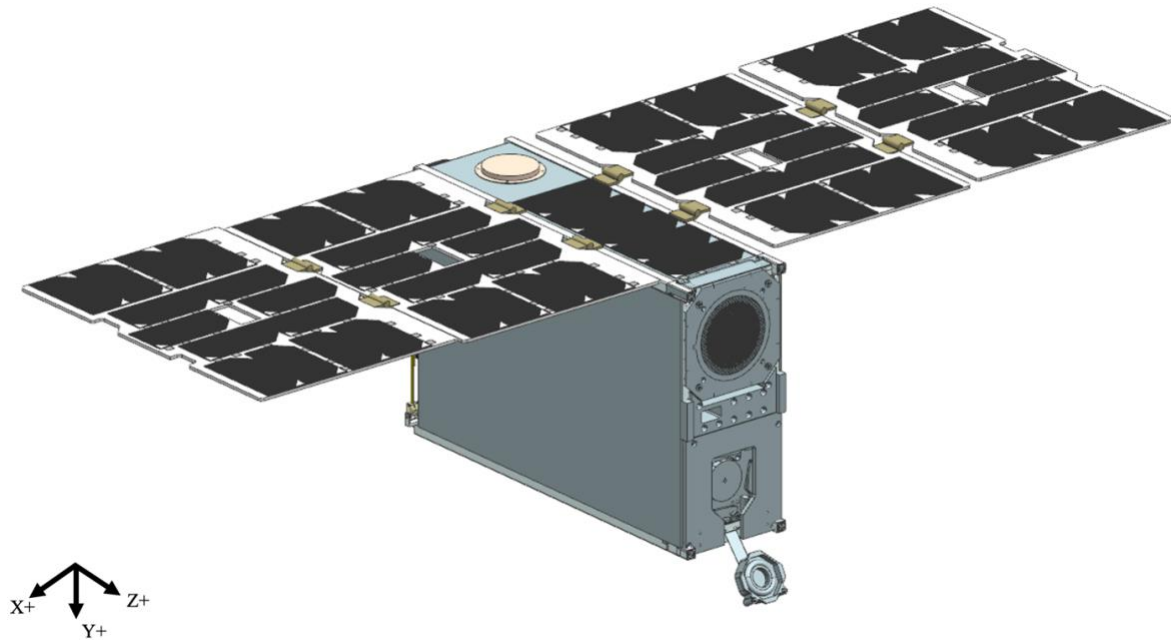
Figure 3: LAICE-F configuration adds double deployable solar arrays to provide sufficient power for the LAICE-F mission payload operations

CHAPTER TWO: LAICE HARDWARE TESTING

Over the summer of 2021, the six solar panels that incorporated the LAICE attitude determination and control system (ADCS) on their internal face were taken out of storage for testing. Limited documentation was available for each panel, and testing and troubleshooting the panels was challenging. The internal face of each panel houses a flex cable, coarse sun sensor, and magnetorquer, and the external face is mounted with solar cells. The X+, X-, and Y+ panels have magnetometers while the X-2 and X+2 panels have gyroscopes. The defined body axes of LAICE are shown in Figure 1, and the order of the X panels are shown below in Figure 4.
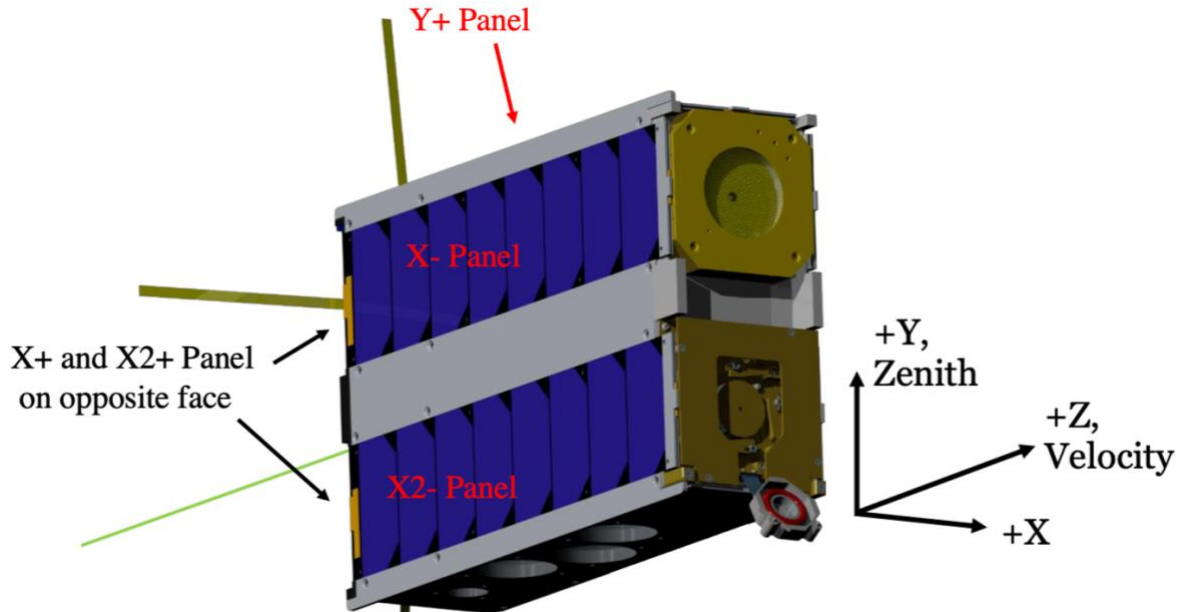
Figure 4: Original LAICE configuration

The testing setup replicated the flight configuration with no electrical or functional differences. Each panel was plugged into the LAICE computer control board, and the magnetorquers (i.e., torque coils), flex cables, coarse sun sensors, and gyroscopes on each panel were tested. An aliveness test was used to determine the status of the flex cable and the sun

sensors. Microcontroller commands were sent to each device on each panel to see how they would respond.
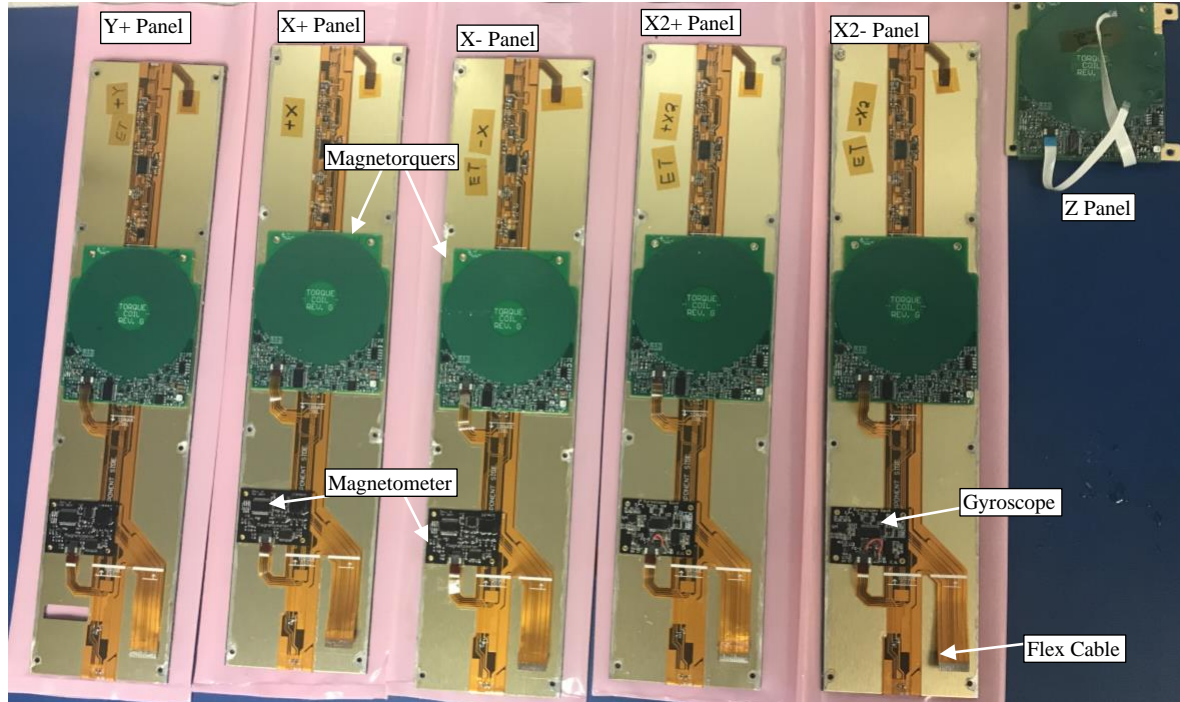
Figure 5: ADCS hardware mounted on backside of solar panels.

Unfortunately, none of the components on the X+ panel responded to commands. On the X- panel, the flex cable and sun sensor responded correctly and were in working condition. The magnetorquer, tested in the positive direction, turned on for 20 seconds and generated a maximum field strength of 1,846 mG with a resolution of ~37 mG. The maximum field strength saturated the magnetometer used for the test in the negative direction but had the same resolution and on-time. Both directions displayed an issue of residual current after reaching maximum field and were unable to zero out. The readings showed 25-40 mG residual field.

After several unsuccessful tests of the magnetometer on the X- panel, it was discovered the magnetometers were pulse triggered, and an external reading was unachievable. Externally generating a sufficiently shaped pulse was not possible in this test set up.

For the Y+ panel, the flex cable and sun sensor responded correctly and were in working condition. The magnetorquer, tested in the positive direction, turned on for 20 seconds and generated a maximum field strength of 1,911 mG with a resolution of ~20 mG. The maximum field strength was 1,948 mG for the negative direction but had the same resolution and on-time.

For the X-2 panel, the flex cable and sun sensor responded correctly and were in working condition. The magnetorquer, tested in the positive direction, turned on for 20 seconds and generated a maximum field strength of 1,990 mG with a resolution of ~30 mG. The maximum field strength in the negative direction was 1,985 mG with a resolution of 20 mG. The gyroscope on this panel turned on but read extremely high rates of rotation at rest and displayed significant variance across multiple readings.

The flex cable on the X+2 panel did not respond, but the sun sensor responded correctly. The magnetorquer on this panel did not respond. The gyroscope on this panel behaved the same as on the X-2 panel, showing extremely high rotation rates at rest with significant variance between readings.

The status for each component is shown in Table 1. Green indicates the component worked as expected, yellow indicates it turned on, but did not work as expected, and red indicates the component did not work. Dark gray indicates the component is unable to be tested with existing testing hardware. The Z panel was not tested.

Table 1: LAICE hardware status

X+ Panel	X- Panel	Y+ Panel	X-2 Panel	X+2 Panel	Z Panel
Flex Cable	Flex Cable	Flex Cable	Flex Cable	Flex Cable	NA
Coarse Sun Sensor	Coarse Sun Sensor	Coarse Sun Sensor	Coarse Sun Sensor	Coarse Sun Sensor	NA
Magnetorquer	Magnetorquer	Magnetorquer	Magnetorquer	Magnetorquer	Not tested
Magnetometer	Magnetometer	Magnetometer	Gyroscope	Gyroscope	NA

The testing of the magnetorquers was alarming in that all panels exhibited the 20 seconds on and then self-shut off behavior. They also saturated before reaching an expected peak value – resulting in a dynamic range that was reduced to 0.3% of the expected range. In addition to this, the timing of the ADCS subsystem presented significant issues. As all ADCS submodules share the same multi-drop serial bus, only one device could be interrogated and a response received at a given time. Multiple devices had to be commanded in series, significantly lengthening the time required to implement control laws. The devices each responded in 200-800 milliseconds, and it took several seconds to poll all sensors and command the magnetorquers in series. A requirement given in the original LAICE CDR from 2014 states, *"Torque coil magnetic field duration must be controllable with a time step of 50 milliseconds or less"*. The tested hardware was unable to meet that requirement.

The principal investigators were informed of the results, and direction to abandon the original hardware and spacecraft design was received. In their place, a new program was defined, repurposing the existing set of instruments for accommodation within a new spacecraft bus designed to satisfy the instrument functional requirements. The maturation of this new mission design is the subject of subsequent chapters.

CHAPTER THREE: MISSION REQUIREMENTS AND PAYLOADS

Concept of Operations

In order to define the system architecture, a concept of operations that implements the defined mission objectives was envisioned. The concept of operations outlines the major functions LAICE-F needs to complete the mission objectives. The LAICE-F mission begins with launching into LEO and delivery to the ISS. LAICE-F is then deployed from the ISS and begins detumble maneuvers to dampen any rotation induced from deployment and stabilize its attitude. After achieving a stable attitude, if LAICE-F is in eclipse, it enters LVLH orientation to begin payload operation. If the satellite is in daylight, it begins to track the sun with the solar panels with only the VT instruments in operation. When passing over the ground station, LAICE-F downlinks data and receives commands. These three modes make up the primary mission and continue until the orbit naturally decays and LAICE-F reenters the atmosphere. The concept of operations is illustrated in Figure 6.
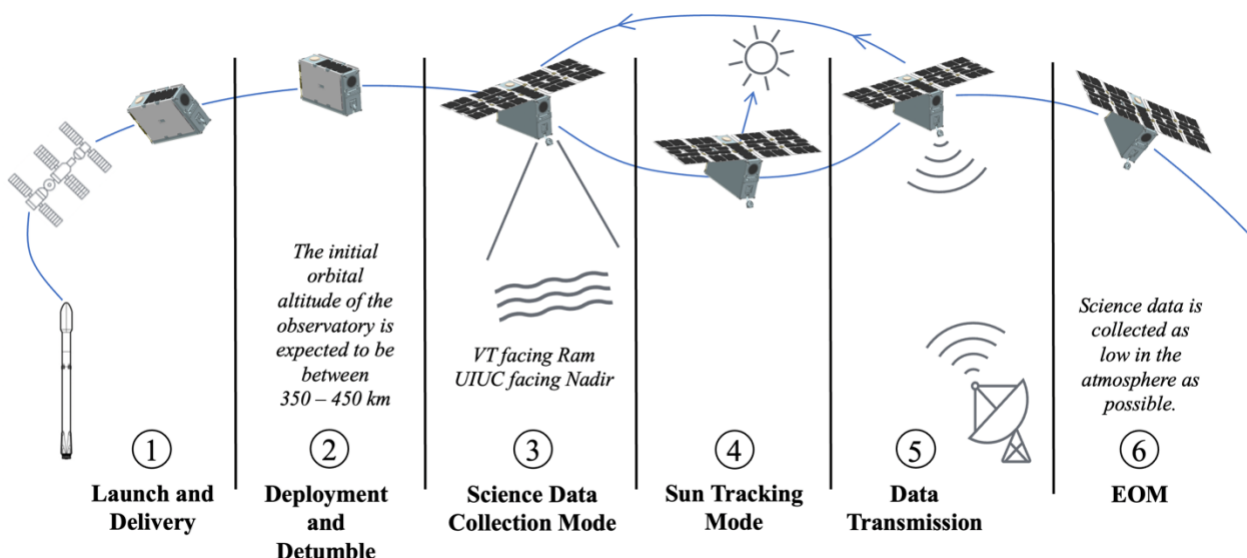
Figure 6: LAICE-F concept of operations

With the concept of operations in place, the LAICE-F mission can be broken down into the specific functions needed to complete the mission objectives. These functions can then be assigned to the physical systems that are able to implement them. With each function assigned to a system, requirements for all systems can be formulated.

The primary systems required for the LAICE-F mission are the launch vehicle, the satellite bus and payloads (observatory), and the ground station. The main function of the launch vehicle is to deliver the observatory to the ISS. The satellite houses the payloads and supplies power, implements commands, collects data, provides an acceptable thermal environment, and orients and stabilizes the spacecraft in the correct attitude. The ground station sends commands and receives data from the satellite. An illustration of the system architecture with the components of each subsystem and how the systems interface with each other can be seen in the interface control diagram (ICD) in Figure 7. This will be used to facilitate the design of the bus and subsystems.
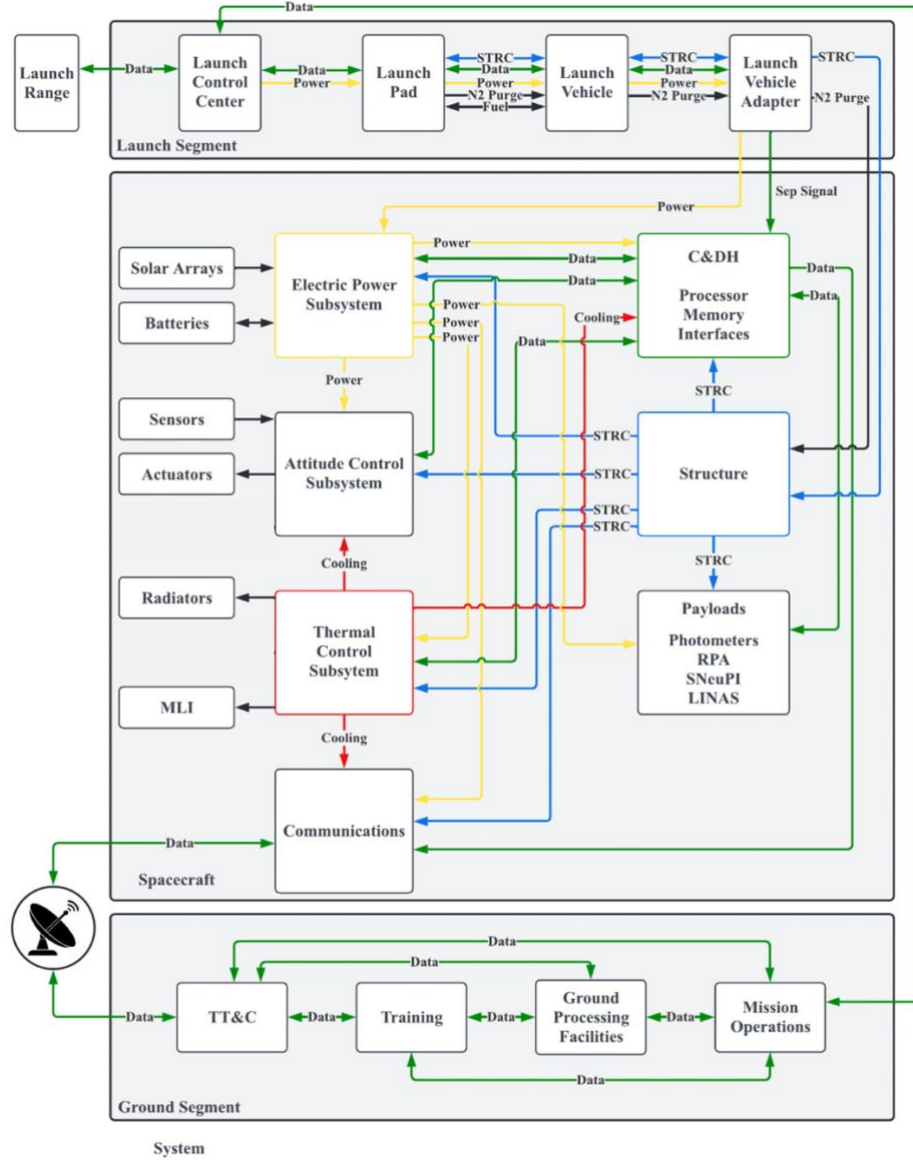
Figure 7: Interface control diagram for LAICE-F

From the concept of operations and ICD the most important requirements for the satellite were derived. These requirements, listed in Table 2, outline the critical functions each subsystem needs to provide to operate. These cover the thermal, attitude determination and control (ADCS), power, communications, and control and data handling (C&DH) requirements. The full documentation of requirements is provided in the *LAICE-F System Requirements Review* (SRR).

Table 2: Most important requirements for observatory

Req #	Requirement	Notes
MIR-1	**The Observatory shall control the attitude in three axes.**	*The Observatory needs to maintain orientation for instrument pointing.*
MIR-2	**The Observatory shall provide pointing knowledge in three axes.**	*The Observatory will have sensors and actuators allowing it to determine its attitude*
MIR-3	**The Observatory shall generate power.**	*After deployment, power must be provided for the mission lifetime*
MIR-4	**The Observatory shall store power.**	*Intended to utilize a battery pack.*
MIR-5	**The Observatory shall distribute power.**	*Intended to regulate and distribute to all subsystems.*
MIR-6	**The Observatory shall store valid data.**	*Implies lower-level requirements on hardware and software for best efforts to return valid data to the ground.*
MIR-7	**The Observatory shall accept commands uplinked from Ground Control.**	*A communication system is required to transfer commands and data from the ground to the Observatory.*
MIR-8	**The Observatory shall downlink data.**	*Data (payload and telemetry) collected onboard the Observatory, is sent to ground control for review.*
MIR-9	**The Observatory shall maintain operating temperatures for all instruments.**	*The Observatory provides an operational environment for the bus and payload instrument.*
MIR-10	**The Observatory shall be designed for a minimum two-year on-orbit lifetime.**	*Basic PI science is achieved at 9 months. Satellite systems are designed for a 2-year design lifetime.*

Instrument Definition and Requirements

As part of the mission feasibility assessment, spacecraft and instrument functional and performance requirements were captured and enumerated in the sections that follow. Only the main requirements for each instrument are listed here. The full documentation is in the SRR.

Photometers

The main objective of the photometers is to determine wave parameters for observed gravity waves. This includes wave amplitude, horizontal and vertical wavelengths, and wave temperature. The photometers (Figure 8), point in the nadir direction (defined as the +Y direction) to observe mesospheric nighttime airglow by photon counting.

Figure 8: Photometers cad rendering (left) and physical hardware (right)

The instrument is composed of seven photomultiplier tubes (PMTs), with each PMT observing at a specific wavelength in either the ultraviolet (UV) or visible spectrum. The airglow the photometer is observing is a semi-stable luminescence caused by chemical reactions in the upper atmosphere, and molecular oxygen (O_2) is one of the principal contributors to this airglow [2]. The main observations are taken at the O_2 atmospheric and O_2 Herzberg emission wavelengths. The UV observation at 280.0 nm is used as a cut-off, as measurements beyond that are not of interest to this study. The longest wavelength observed, 770.0 nm, is used for a background measurement. Each channel has a 1.5° field of view (FOV) with a 12 x 20 km footprint at 95 km altitude with a one second integration time. The location of each specific tube is adjustable and multiple configurations were examined in CAD. For each PMT listed in Figure 8, the corresponding wavelength it observes is given in Table 3.

Table 3: Photometer tubes and corresponding wavelengths

Photomultiplier Tube	Measured Wavelength (nm)
A1	760.2
A2	760.4
UV	280.0
BG	770.0
A3	760.8
B	764.9
A4	760.9

The horizontal and vertical wavelengths and phases of the gravity waves can be determined from the change in intensity of the O_2 Herzberg and O_2 A emission lines, as illustrated in Figure 9.
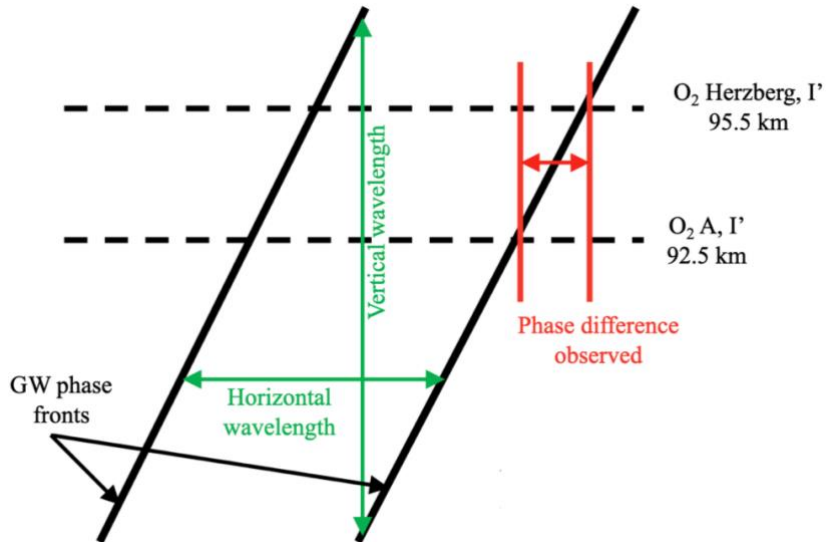
Figure 9: Gravity wave phase fronts and wavelengths vs. altitude

Due to the sensitivity of the PMTs, the photometer operates only during eclipse, so that the optics are not damaged by sunlight. The photometers also need to be aligned to nadir within $10°$, to obtain the useful measurements. The requirements for the photometers are listed in Table 4.

Table 4: Main requirements for photometers

Req #	Requirement	Notes
PHO-1	**The Photometers shall collect measurements of nighttime airglow perturbations in the upper mesosphere.**	*A principal mission objective is to measure remote airglow perturbations.*
PHO-2	**The Photometers shall operate during eclipse.**	*The payload measures nighttime airglow brightness.*
PHO-3	**The Photometers shall be aligned to nadir $\pm 10°$ during operation.**	*This requirement feeds into the ACS system.*
PHO-4	**The Photometers shall be kept pointed ≥ 23 degrees away from the sun.**	*This requirement eliminates any first reflection, as sunlight will damage photometers. Only available when ACS is active.*

Since the payload hardware was built for the original LAICE and hardware exists, the key parameters for the photometers are accurately known and given below in Table 5. These values feed into the power and communications analyses, and the volume and mass budgets.

Table 5: Critical parameters of the photometers

Photometers	
Volume	2178.450 cm^3
Mass	1563.9 g
Data Rate	21 bytes per second
Standby Power	0.12 W
Operational power	2.70 W
Duty Cycle	33% (Average over one orbit)

VT Instruments

The VT instrument suite is comprised of three in-situ instruments: the RPA; LINAS; and SNeuPI. The RPA design has been flown in space for over 45 years [3]. LINAS is a Bayard-Alpert type gauge that has been scaled down from previous space missions [4]. SNeuPI is a technology demonstration that will take the same measurements as LINAS but with lower mass and power requirements.

The RPA, shown below in Figure 10, measures plasma density and ion temperature, as well as ion velocity in the ram (i.e., along orbit track) direction. The RPA is made of multiple fine mesh grids stacked between a planar collector and aperture grid. One grid sweeps across different voltages, while the others and collector are kept at constant but unique voltages. The first grid is held at spacecraft ground, to even out small variations in the incoming plasma and ensure the other grid potentials do not interfere with the measurement. The second grid removes electrons from the plasma so the ions can be observed. The remaining grids increase in voltage which allows only high energy ions through [5].
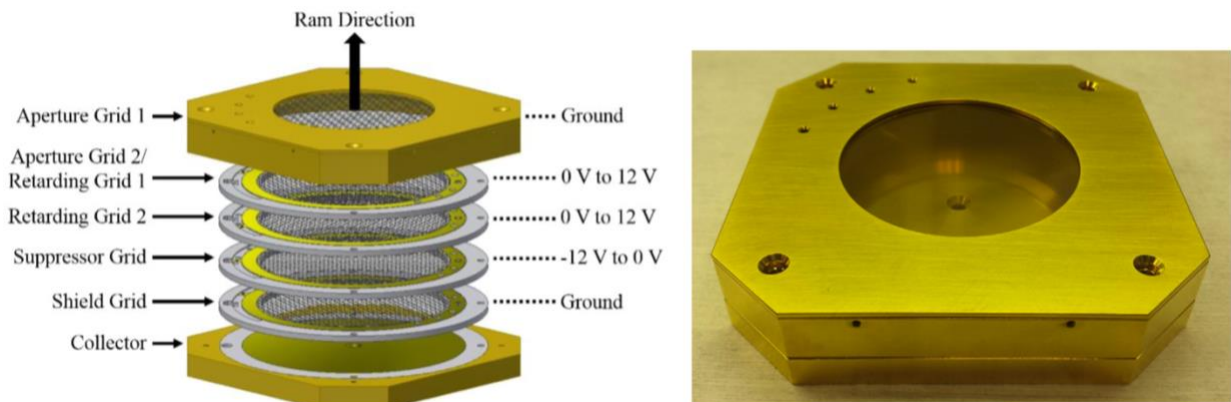
Figure 10: RPA CAD rendering (left) and hardware (right)

The vertical movement of gravity waves in the ionosphere is related to changes in the plasma density and ion temperature [6]. Since the RPA can complete one voltage sweep in one

second, it can produce a horizontal spatial resolution of 8 km, which is sufficient for the mission.

The requirements for the RPA are given below in Table 6.

Table 6: Main requirements for RPA

Req #	Requirement	Notes
RPA-1	**The RPA shall measure in-situ plasma density.**	*A principal mission objective is to measure plasma density.*
RPA-2	**The RPA shall measure in-situ ion temperature.**	*A secondary mission objective is to measure ion temperature.*
VT-1	**VT Instrument Suite shall be aligned to ram $\pm 10°$.**	*This requirement feeds into the ADCS system*

LINAS and SNeuPI, seen below in Figure 11, are housed in the LAICE accommodation chamber with a shared aperture and measure neutral gas density. SNeuPI, a prototype instrument, will use measurements from LINAS for validation. Once SNeuPI measurements are confirmed to match LINAS, LINAS may be turned off to reduce power consumption.
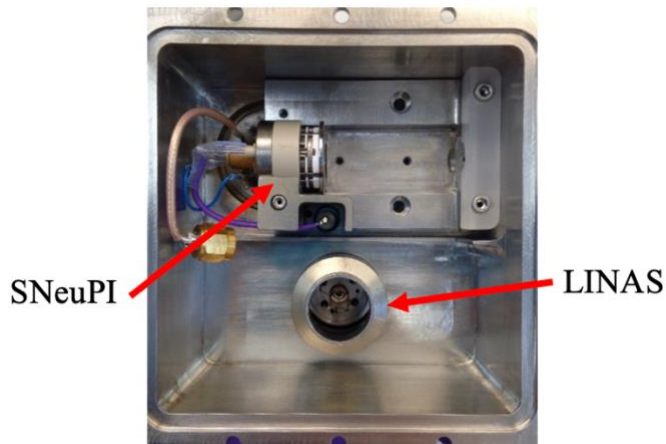
Figure 11: SNeuPI and LINAS in LAICE-F accommodation chamber

SNeuPI measures ion density using a micro-channel plate (MCP), aperture, baffle, and microtip electron emission source. The emitter tips ensure electrons with energies corresponding

17

to the voltage pass through the emitter gate. As electrons enter the chamber, they decelerate as they approach the MCP. They are then repelled and absorbed by the grounded walls. This allows the neutral gas molecules that enter through the aperture and baffle to be ionized. MCP acts as a current multiplier, and the current measured at the output is proportional to the number of ions at its input. The neutral gas density can then be measured from the number of ions [4]. The main requirements for SNeuPI are given below in Table 7.

Table 7: Main requirements for SNeuPI

Req #	Requirement	Notes
SNP-1	**SNeuPI shall measure in-situ neutral gas pressure.**	*This is a main objective of LAICE-F.*
VT-1	**VT Instrument Suite shall be aligned to ram $\pm 10°$.**	*This requirement feeds into the ADCS system*

LINAS uses a Cannon MG-2 Bayard-Alpert ionization gauge, and measures neutral gas density by partially ionizing a volume of gas and measuring the resulting current from the ions collected by the biased collector. The ratio of the collected ion current to the ionizing electron current is proportional to the density of gas in the chamber. LINAS is also able to calculate neutral ion temperature from the pressure measurements [4]. The requirements for LINAS are shown below in Table 8.

Table 8: Main requirements for LINAS

Req #	Requirement	Notes
LNS-1	**LINAS shall measure in-situ neutral gas pressure.**	A principal mission objective is to measure neutral gas pressure.
VT-1	**VT Instrument Suite shall be aligned to ram $\pm 10°$.**	This requirement feeds into the ACS system.

The CAD rendering and hardware of LINAS and SNeuPI are shown in Figure 12. The aperture to the instruments is protected from dust and water vapor prior to deployment by a cover mechanism that is vacuumed sealed. Once LAICE-F is stabilized in its orbit, the cover is released by thermal knives cutting through a restraining "string."
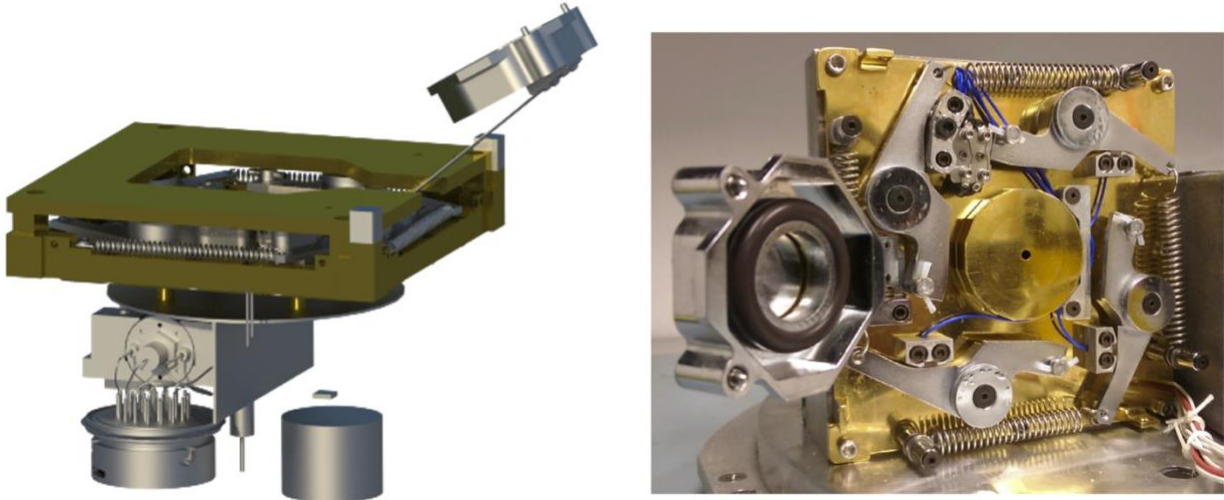
Figure 12: CAD rendering (left) and hardware of LINAS and SNeuPI

The important parameters for the suite of VT instruments are given below in Table 9.

Table 9: Critical parameters for VT payloads

VT Instruments' Parameters	
Volume	$3,696.461 cm^3$
Mass	3200 g
Data Rate	338 bytes per second
Standby Power	3.17 W
Operational power	8.65 W
Duty cycle	100%

In order to support the payloads primary functionality, a set of software modes and tasks was defined for implementing that functionality (Table 10). These are derived from the concept

of operations outlined in Figure 6, and each mode covers the tasks required for LAICE-F to

maintain on-orbit operations.

Table 10: Software modes and tasks

Mode	Tasks	Description
Start-Up	Detumbling	Start ADCS detumbling routine.
	Commissioning	Start Construct Health Status Packet routine and send packet to radio.
Power Management and Monitoring	Monitor Battery Levels	Monitor Battery Levels and enter Critical Battery State if necessary.
	Critical Battery State	Save batteries by turning off or putting devices in standby, as needed.
	Monitor Solar Panels	Monitor solar panel's health via changes in expected output power.
Receive Packets	Get Packet	Receive packet from radio and acknowledge. Start Parse Packets routine.
Parse Packets	Payload Commands	Schedule Payload Start routine with command specified configuration.
	Status Command	Start Construct Health Status Packet routine and send packet to radio.
Flight Computer Error	Collect Current State	Collect and record flight computer state and general system state.
	Trigger General Error	Start General Error routine.
General Error	Automated Error Resolution	Attempt checks to resolve error without communication to ground station.
	Construct Packet	Create packet with error information and send to S-band radio.
	Parse Packet	Receive packet with error resolution information from radio and parse information packet.
	Execute Resolution	Attempt error resolution based on ground commands.

Similarly, tasks necessary for the payload controller to complete were written. The payload controller provides an interface between the bus and the payloads and manages all the tasks required for the payloads to operate. These tasks are separated into four modes and are listed below in Table 11.

Table 11: Payload controller states and tasks

State	Tasks	Description
Calibration	ADCS Pointing Confirmation	Bus orientation is ready for payload operation.
	Payload Start	Provide operational power to the Payload.
	Payload Calibration	Begin science routines.
Science Data Management	Data Collection	Retrieve data generated from payload.
	Off-Payload Processing	Process data from payloads into appropriate formats.
	Save Data	Save data to memory for downlink.
Send Packet	Construct Status Packet	Create packet containing health and status information.
	Construct Science Data Packet	Create packet containing saved science data.
	Send Packet	Send status or data packet to S-band radio.
Payload Controller Error	Collect Current State	Collect payload controller state and general system state.
	Trigger General Error	Start General Error routine.

CHAPTER FOUR: ORBITAL CONFIGURATION AND POWER ANALYSIS

The objective of the orbital configuration and power analysis was to analyze the orbital and physical configurations for feasible power generation options. The orbital analysis for LAICE-F starts with the assumption of all initial orbital parameters matching the ISS, (based on deployment from the ISS). This constrains the inclination and initial altitude of LAICE-F to 51.6° and approximately 420 km [7]. LAICE-F uses solar panels to generate power from the sun and stores energy in an on-board battery pack for operation during eclipse. A maximum power point tracker (MPPT) adjusts the generated voltage and current to maintain peak power output.

There are two main power modes for LAICE-F. The first is daylight mode, when LAICE-F is receiving power on the panels, VT instruments are on, and the photometers are off. The second is eclipse mode, when LAICE-F is in eclipse and no power is generated, and all payloads are on. In daylight mode, the solar array needs to produce enough power to power the bus and VT instruments and charge the batteries. During eclipse, the batteries must provide enough power to keep the bus and all payloads on. A schematic of this model is shown in Figure 13.
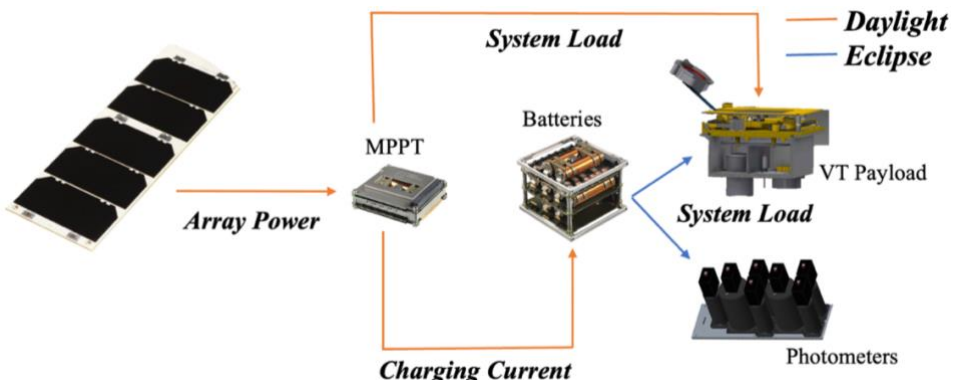
Figure 13: Schematic of power model showing daylight and eclipse loads

The first step to sizing the power system is to analyze the power budget for the satellite. The power budget is comprised of the power requirements for each component on LAICE-F. Table 12 gives the current, voltage, power, and duty cycle for each bus component.

Table 12: Subsystem Power Budget

Component	Current (A)	Voltage (V)	Power (W)	Qnt	Power (W)	Duty Cycle (%)	Average Power (W)
Flight Computer	0.1	3.3	0.33	1	0.33	100%	0.33
Payload Controller	0.075	3.3	0.24	1	0.24	100%	0.25
Electrical Power Distribution Unit	0.0455	3.3	0.15	1	0.15	100%	0.15
Battery Heaters	0.1	3.3	0.33	4	1.32	100%	1.33
Magnetorquers	0.121	3.3	0.39	6	2.34	50%	1.20
Reaction Wheel (Steady State)	-	-	0.15	4	0.6	100%	0.60
Sun Sensors	0.01	5	0.05	6	0.3	100%	0.30
GPS Receiver	0.0378	3.3	0.12	1	0.12	100%	0.12
GPS Antenna	0.02	3.3	0.07	1	0.07	100%	0.07
IMU	0.3	5	1.50	1	1.5	100%	1.50
UHF Rx	0.05	3.3	0.17	1	0.17	100%	0.17
UHF Tx	2.45	3.3	8.09	1	8.09	1.11%	0.09
S-Band Tx	1	5	5.00	1	5	1.11%	0.06
Totals		Max Instantaneous Bus			**20.23**	Nominal Bus Total	**6.11**

The instantaneous maximum bus power required for LAICE-F was calculated to be 20.23 W. This is for all components on, including the UHF transceiver and receiver, and S-band transceiver. This is the maximum power the bus will ever be required to produce. The situation

where this would happen would be the magnetorquers having to complete a momentum management maneuver during a communications pass.

When duty cycles are considered for the radios and magnetorquers, an estimate is made for the nominal bus total for one orbit. The duty cycles are based on nominal downlink requirements and best estimates for magnetorquer momentum management maneuvers. The nominal bus total is 6.11 W. The power requirements for payloads are given below Table 13.

Table 13: Payload power budget

Payload (Mode)	Power (W)	Duty Cycle (%)	Total Power (W)
Photometer (Standby)	0.12	~66%	0.12 (daylight load)
Photometer (Operation)	2.70	~33%	2.70 (eclipse load)
VT (All Standby)	3.17	0%	3.17
VT (All in Operation)	8.65	100%	8.65
SNeuPI (Operation)	4.58	100%	4.58
LINAS (Operation)	6.28	100%	6.28
RPA (Operation)	4.95	100%	4.95
Sunlight Payload Power	8.77	Eclipse Payload Power	11.35

For the payloads power budget, the duty cycles are based on the operational requirements of continuous VT payload operation and the photometers being operational only in eclipse. Therefore, the sunlight payload power load is the sum of the power consumed by the photometer in standby mode and the VT payloads in operation. Similarly, the eclipse payload power load is the sum of the power required for both the photometers and VT instruments in operation. The values provided for each individual VT instrument is for only a single instrument in operation, with the other two in standby mode. After confirming duplicative functions are working in the

24

VT payloads, LINAS may be powered off for additional power margin. The maximum power LAICE-F will need to provide in daylight and eclipse (Table 14) is the daylight payload power plus the maximum bus power and the eclipse payload power plus the maximum bus power, respectively. The power system must support a peak power usage of 31.58 W for a communications session during eclipse.

Table 14: Nominal and peak power in daylight and eclipse

Power Requirement	Watts
Peak in Eclipse	31.58
Nominal in Eclipse	17.46
Peak in Daylight	29.0
Nominal in Daylight	14.88

As LAICE-F decays in its orbit, the duration of eclipse increases as the duration of daylight decreases. Therefore, the daytime peak energy usage occurs at deployment, or beginning-of-life (BOL), when the days are longer, while the eclipse peak energy usage is at end-of-life (EOL). Since the battery needs to provide power for the duration of eclipse, it should be sized based on the length of eclipse at EOL. The change in daylight and eclipse times are shown in Table 15. The solar array design must account for peak power requirements and battery charging over the mission lifetime.

Table 15: Duration of daylight and eclipse at launch and end of life

	At Launch (BOL)	At End of Life (EOL)
Daylight Duration	0.983 Hrs	0.903 Hrs
Eclipse Duration	0.575 Hrs	0.596 Hrs

Using the maximum duration of daylight/eclipse and the peak power requirement for daylight/eclipse in Table 15, the peak energy usage in daylight and eclipse can be calculated (Table 16). This is found from the longest duration of daylight or eclipse, and the peak power requirement in daylight or eclipse.

Table 16: Peak energy usage in daylight and eclipse

	Energy Use	WHrs
Eclipse	Nominal Energy Usage (EOL)	10.41
	Peak Energy Usage (EOL)	18.82
Daylight	Nominal Energy Usage (BOL)	14.63
	Peak Energy Usage (BOL)	28.51

To begin sizing the battery, the depth of discharge (DOD) acceptable for the mission lifetime needs to be determined. Each battery charge-discharge cycle uses up a small amount of capacity that the battery can provide over its lifetime. The DOD is the percent that a battery is discharged. Typically, the depth of discharge is limited to ~30% for a satellite in LEO [8]. To find an acceptable depth of discharge, the number of cycles the battery goes through in its lifetime is needed, and therefore an accurate estimate for the lifetime of LAICE-F must be provided.

An orbital mechanics simulation tool, FreeFlyer provided by a.i. Solutions, was used to create a model of the power system and its operating environment, including the battery, solar array, and various pointing/attitude schemes. FreeFlyer was able to produce orbital decay and lifetime estimates, a power budget, provide information on limitations on the power generation and solar array and battery sizing, as well as inputs for thermal and communication analysis.

FreeFlyer's estimate for the satellite lifetime is computed by an orbital decay model which included atmospheric drag and J2 perturbations. Assuming a launch date of January 1, 2025 at 420 km, the end of mission (defined as the day LAICE-F's orbit decays to 250 km altitude) is August 17, 2027, or 958 days later. Over this duration, 91.6% of orbits have eclipses greater than 15 minutes. With nominal solar weather environments, LAICE-F is expected to have a 2-3 year lifetime.
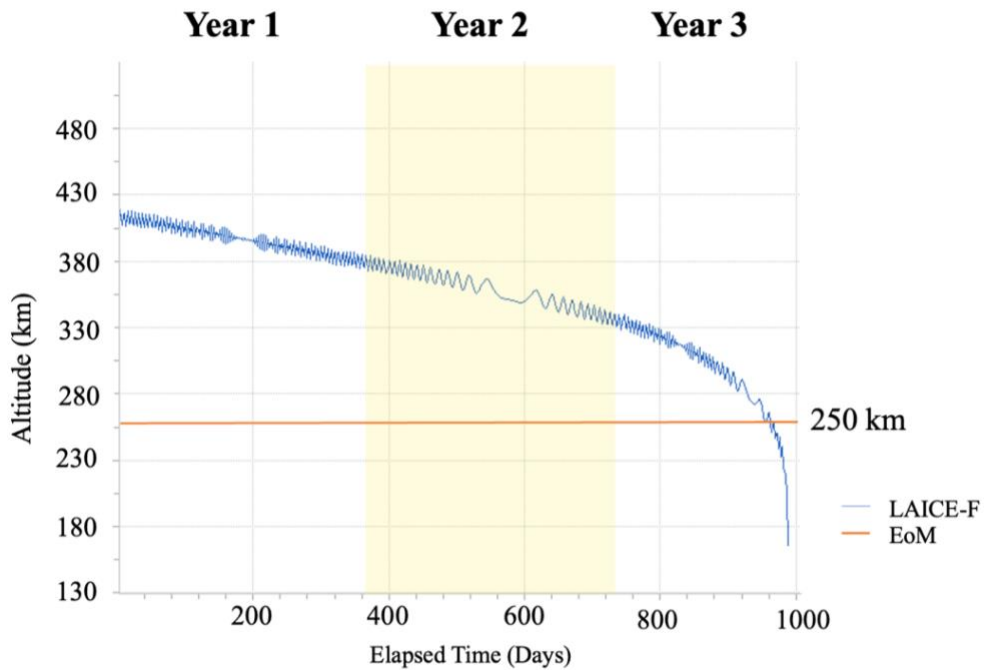
Figure 14: Orbital decay of LAICE-F over 3 years [9]

Over two years, the batteries complete 10,950 cycles. From Figure 15, the maximum desired DOD is approximately 25%.
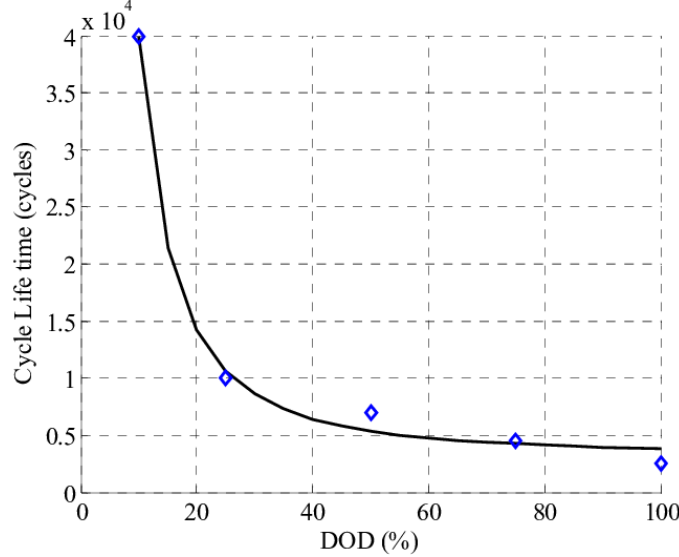
Figure 15: Optimal battery depth of discharge vs. number of cycles [10]

Now the energy the battery needs to have to power LAICE-F during eclipse while not exceeding a 25% DOD can be found using the power load during eclipse (P_L), the time in eclipse (T_E), and depth of discharge, shown in Equation 1.

$$E_b = \frac{P_L T_E}{DOD} \tag{1}$$

Using the nominal eclipse load, the battery would need to be capable of storing 41.62 Whrs. Using the peak eclipse load, the energy the battery needs to store to remain at or above the 25% DOD is 75.29 Watt Hours. The initial analysis was for a battery sized for the nominal eclipse load, because of the infrequency and short duration of communications sessions.

Using NanoAvionics stock electrical power system, each battery cell has an energy capacity of 11.59 Whs [11]. Therefore, the battery pack able to support the nominal eclipse power load needs to contain four battery cells. This is referred to as a "single" battery with its characteristics given in Table 17.

Table 17: Single battery parameters

Single Battery Pack Characteristics	
Nominal Energy Used in Eclipse	10.41 WHrs
Battery Single Cell Capacity	11.59 WHrs
Battery Four Pack Capacity	46.36 WHrs
Expected Battery DoD	22.45%

Continuing onto the solar panel design, the power generated by a solar panel can be found using Equation 2:

$$P = S_c \sin(\beta) \, A \, e \qquad\qquad (2)$$

The variable P is the power generated in Watts, S_c is the solar constant at 1AU (known to be 1350 W/m^2), β is the angle between the incident sun vector and the solar panel, A is the total area of the solar cells in m^2, and e is the efficiency of the solar cells. The maximum power is when $\beta = 90°$. The largest side of LAICE-F can fit 14 Azure Space high performance solar cells for a total of approximately 0.046 m^2, and with a cell efficiency of 30%, this solar panel could produce a maximum power of 18.8 W [12].

Unfortunately, this configuration is unable to support the peak power requirements outlined in Table 14, therefore, a larger array is required. If LAICE-F is provided with deployable solar arrays, with a panel on each side and solar cells on the anti-nadir face, the area available to produce power will more than double. This array configuration will be referred to as "dual single deployable arrays", as there is a single deployable panel from the anti-nadir face of LAICE-F in the X- direction and one in the X+ direction. This configuration increases the maximum power to 38.9 W. The parameters for this configuration are shown in Table 18.

Table 18: Dual single deployable solar array description

Configuration	Cells	Watts/Cell	Max Power	Energy/Orbit
2 X 1 Deployable Solar Panels in a LVLH attitude	28 (panels) + 7 (body) = 33 (total)	1.179 (30% efficiency)	38.907 W	19.99 WHrs

After modeling this configuration in FreeFlyer, it was observed that the solar panels were generating more power than the batteries could store for parts of the year, as shown in Figure 16.
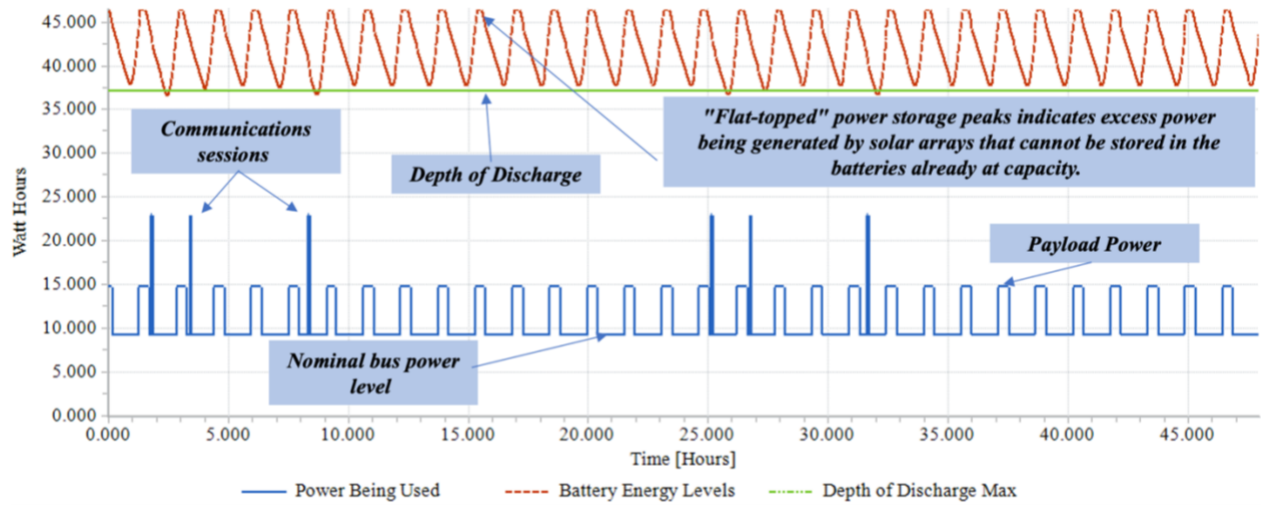
Figure 16: Dual single arrays/ single battery

The flat top of the battery energy level curve indicates that the battery cannot store any more power, yet the solar arrays are still producing power. This simulation was run for a period of 2 days. When the run time was increased to a year to see how the power system performed, the depth of discharge greatly exceeded the desired maximum, shown in Figure 17.
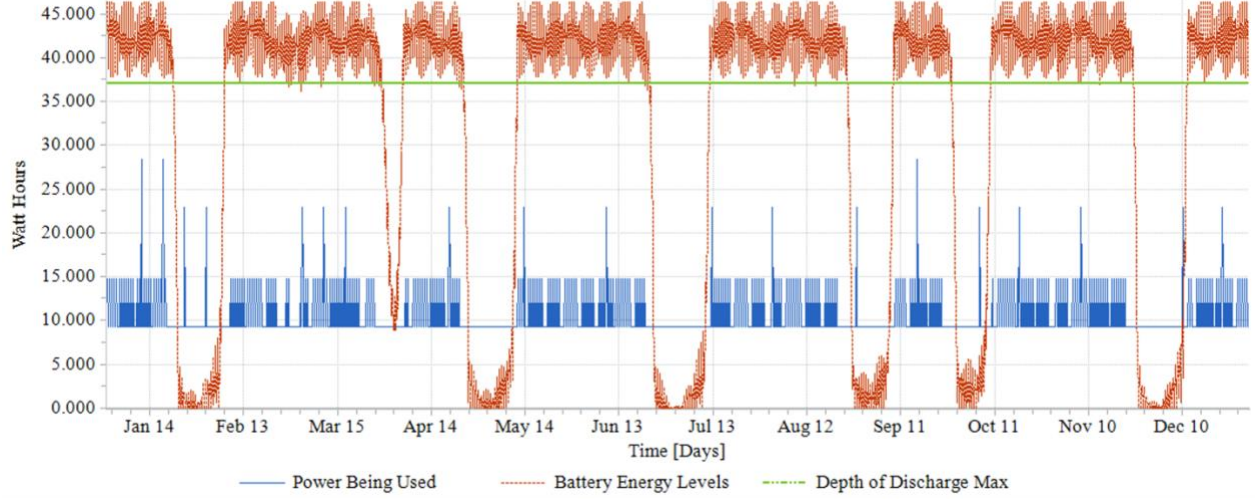
Figure 17: Yearlong analysis of single/single configuration

When the simulation is run for one year, durations of minimal power availability occur with no power from the arrays for charging and the battery drains completely. LAICE-F is orbiting in a LVLH attitude in an inclined orbit, and the oblateness of the earth causes the right ascension of the ascending node (RAAN) to precess throughout the year, a phenomenon known as the regression of nodes [13]. This causes β to vary sinusoidally between 0° and 90°. When LAICE-F's orbit aligns with the terminator (the separation between light and shadow on Earth's surface) and the solar arrays are edge on to the sun ($\beta = 0°$) no power is produced. When the orbit is perpendicular to the terminator ($\beta = 90°$), maximum power is produced. A visual representation of this can be seen in Figure 18.
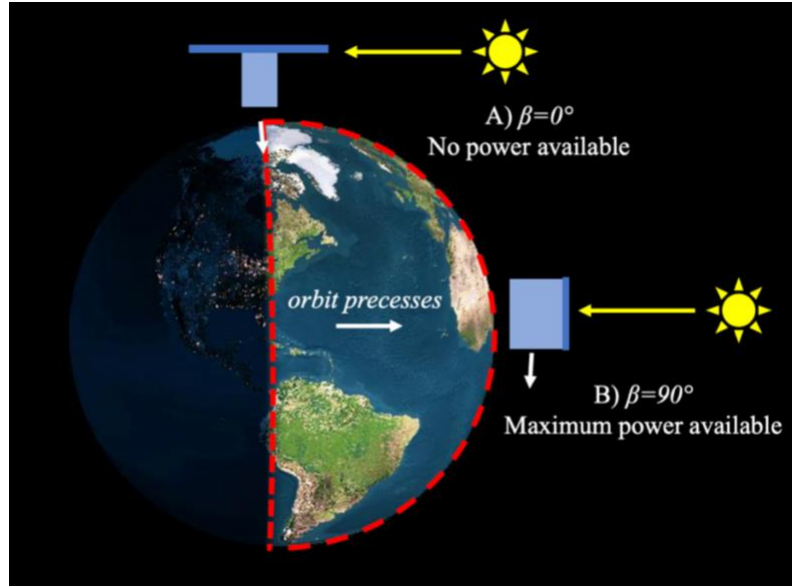
Figure 18: Visualization of LAICE-F panel orientation relative to sun

To address the first issue seen in this array/battery configuration, a battery with a higher capacity was needed. This is to ensure all of the available charging power generated by the panels can be stored, and this also considers the maximum energy needed for eclipse, instead of the initial nominal value used for the first calculation. Therefore, a second configuration that included eight battery cells was modeled, referred to as a "double battery pack." The relevant characteristics of this battery are listed in Table 19.

Table 19: Double battery pack

Double Battery Pack Characteristics	
Maximum energy used in eclipse	18.86 WHrs
Individual battery cell capacity	11.59 WHrs
Maximum desired DoD	25%
Battery cells needed	8
Battery capacity	92.72 WHrs
Expected battery DoD	20.28%

This model also had a set of single deployed solar arrays and was orbited in LVLH attitude. As this configuration was able to store all the power that the panels generated, it maintained a higher DOD during the power-available seasons, as seen in Figure 19. The battery energy level stays above the maximum DOD for the two day period shown. However, the panels do not supply enough energy to run the bus and completely refill the batteries on every orbit. The battery is being recharged, but does not reach 92.72 WHr capacity again.
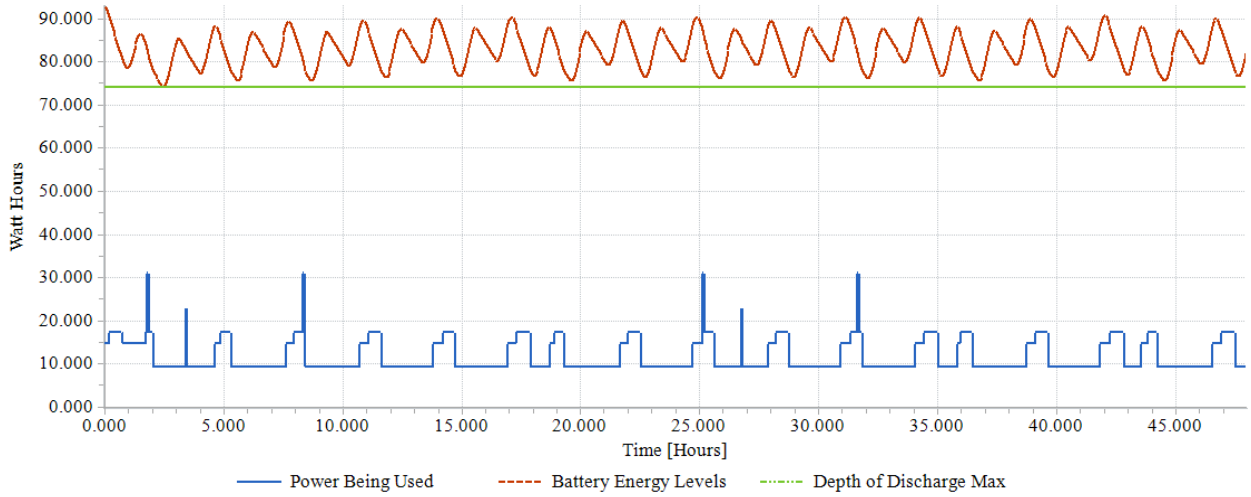
Figure 19: Dual single deployable array with double battery pack

Again, this configuration suffers from the "dead zones" as a result of the regression of nodes seen in the previous analysis, and the battery energy levels drop to zero. The yearlong simulation is shown in Figure 20.
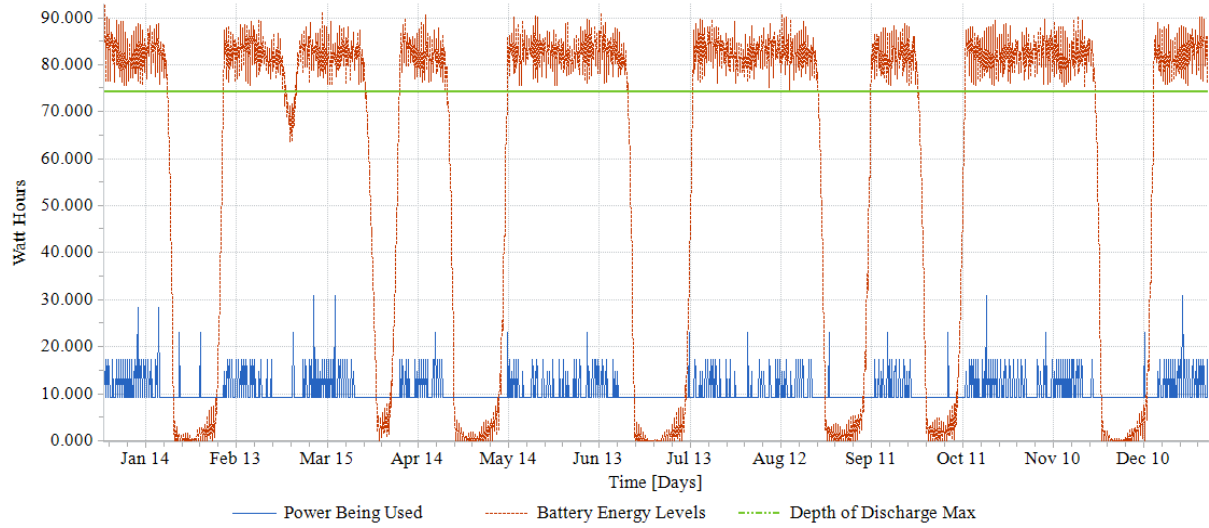
Figure 20: Dual single deployable arrays and double battery over one year

The payload availability for this configuration can be calculated as the percent of desired payload operating time the payloads can actually be powered on for. (i.e., 100% payload availability for VT instruments means the payload is in continuous operation, while 100% payload availability for the photometers means the payload is operation for the entirety of eclipse.) The availability for this configuration over one year is tabulated in Table 20.

Table 20: Payload availability over one year for single array double battery configuration

Payload	Payload Availability
VT	19.32 %
UIUC	36.33%

These numbers represent low availabilities, so a final configuration operating in LVLH attitude was modeled. This configuration uses a double (four panel) deployable solar array with a double battery pack. The panel characteristics are given in Table 21.

Table 21: Double deployable panel parameters

Configuration	Cells	Watts/Cell	Max Power	Energy/orbit
2 X 2 deployable panels	56 (panels) + 5 (body) = 61 (total)	1.179 (30% efficiency)	71.919 W	36.96 WHrs (no sun tracking)

This configuration encounters the same issues observed in the first configuration modeled, shown in Figure 16, where the battery reaches full charge while LAICE-F is still in daylight, but all of the excess power produced by the panels is not stored. The energy profile shown over two days (Figure 21) finds the battery energy level flat-lining at the top, as it is unable to store any more power.
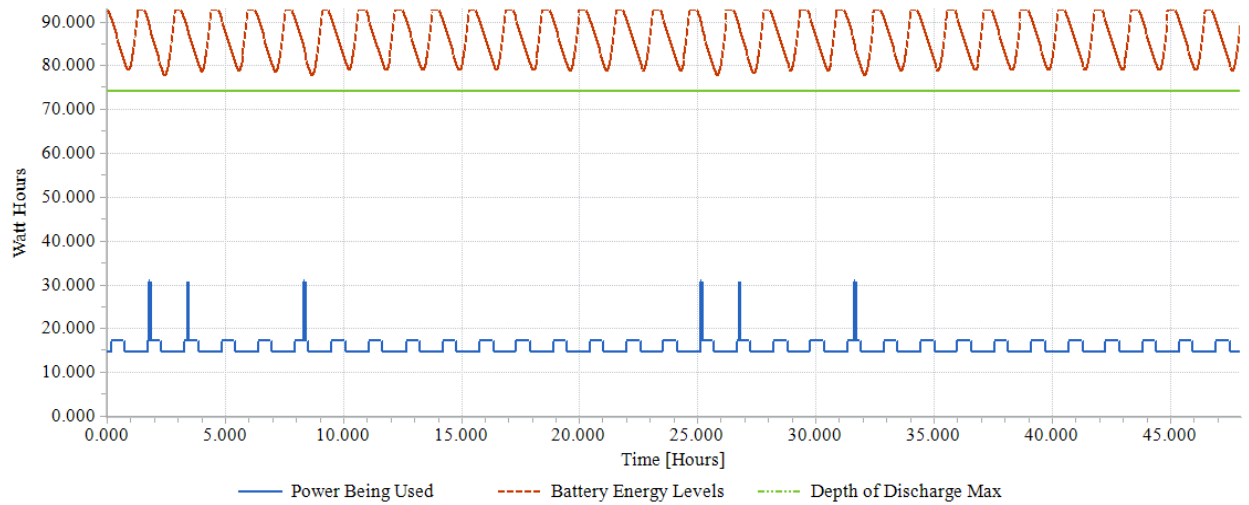
Figure 21: Double deployable arrays/double battery energy profile over two days

The extra power that the arrays are producing that is not being used is shunted and lost to thermal energy. Using a double deployable solar panel and a double battery pack allows for continuous payload operation for most of the year, yet in a LVLH attitude, once again LAICE-F once again faces the issue of loss-of-power during dead zones, as illustrated by the battery draining to zero in the yearlong simulation shown in Figure 22. These are much shorter in

duration than the dead zones observed with the single array configuration, but nonetheless, the power is not sufficient to maintain bus operations throughout the year.
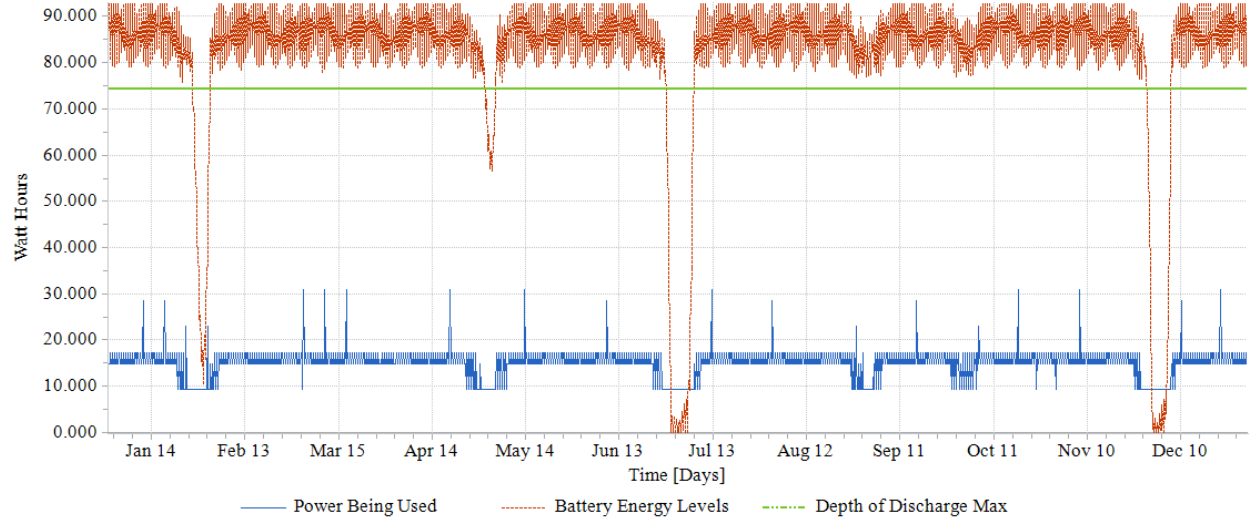
Figure 22: Yearlong simulation for double deployable panels and double battery

The payload availability for this configuration (Table 22) is significantly improved over that achieved with only a single array deployed from each side of the satellite, with VT payload availability increasing from 19.32% to 85.39%, and UIUC payload availability increasing from 36.33% to 96.04%.

Table 22: Payload availability for double array double battery

Payload	Payload Availability
VT	85.39 %
UIUC	96.04%

However, it is desirable that the payload availability for all instruments be 100%. To achieve this, sun tracking is implemented into Free Flyer to analyze the expected improved power collection capability. Due to the requirement that the VT instrument suite must face the

ram direction, LAICE-F rolls about the longitudinal axis allowing the solar panels to point directly towards the sun. As a result, the inactive photometers roll off nadir away from the sun. The sun tracking algorithm slews the satellite only if sunlight is hitting the underside of the solar panels or if the bus is not in shadow, otherwise the photometers will be pointing nadir.

To examine the impact of sun tracking, a single solar panel with a double battery pack was simulated, as the single array/single battery configuration is already known to max out the battery pack. A typical day during the power available season is shown below in Figure 23. This is the same array and battery shown Figure 19, with sun tracking now applied. Sun tracking helps the battery performance, as energy level stays above the minimum state of charge. For this case, VT instruments are always on, and the photometers are on in eclipse.
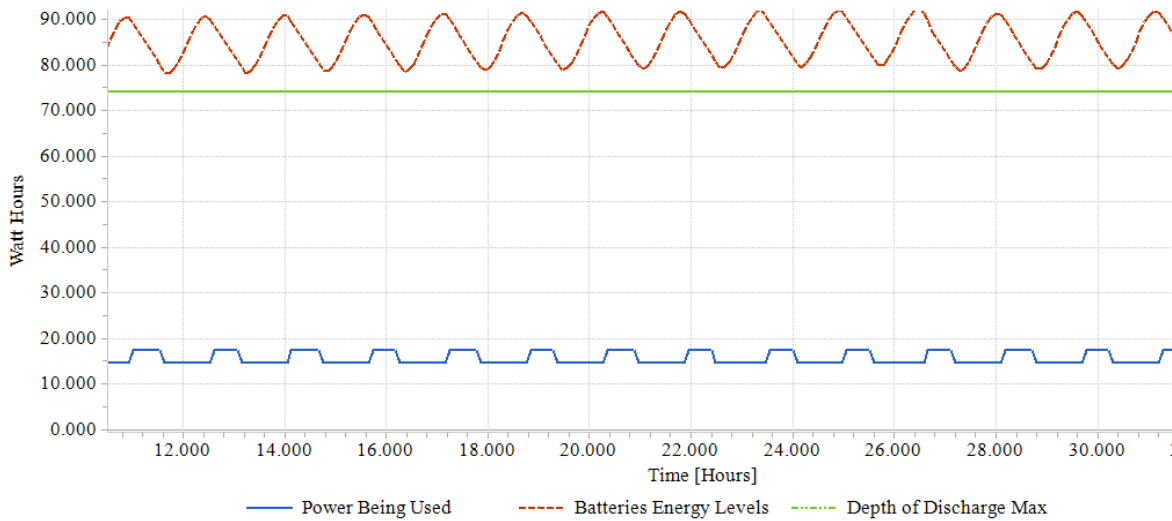
Figure 23: Dual single deployable arrays/double battery pack with sun tracking

During most of the year, LAICE-F can now be run continuously with dual single deployable solar panel and a double battery pack. However, for short periods throughout the year, two orbits of science operation are possible before a one orbit break is required to recharge the batteries. This recharging period is seen below in Figure 24, where the instruments are turned

37

off for an orbit to charge the batteries. These periods align with the dead zones seen in the LVLH analysis, but now LAICE-F can maintain a low, but non-zero β angle.
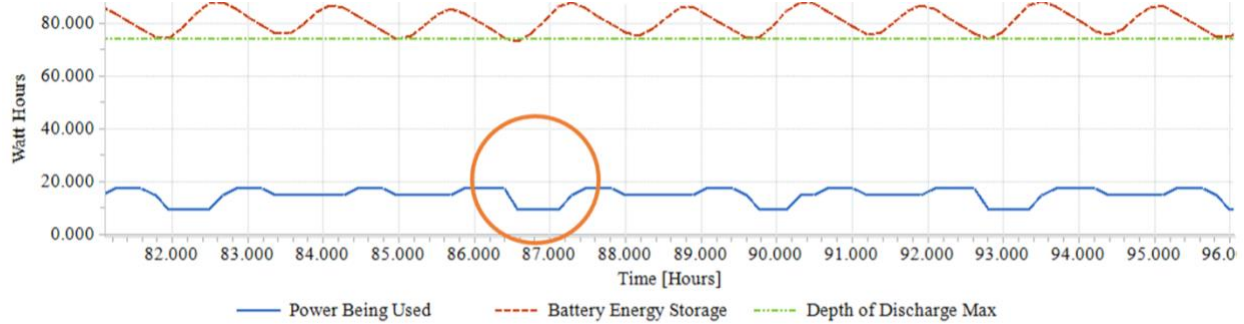
Figure 24: Dual single deployable arrays/double battery pack with sun tracking with recharge necessary

The yearlong simulation is shown in Figure 25, where it can be seen that there are several instances during the low power times where the battery level decreases past the maximum DOD.
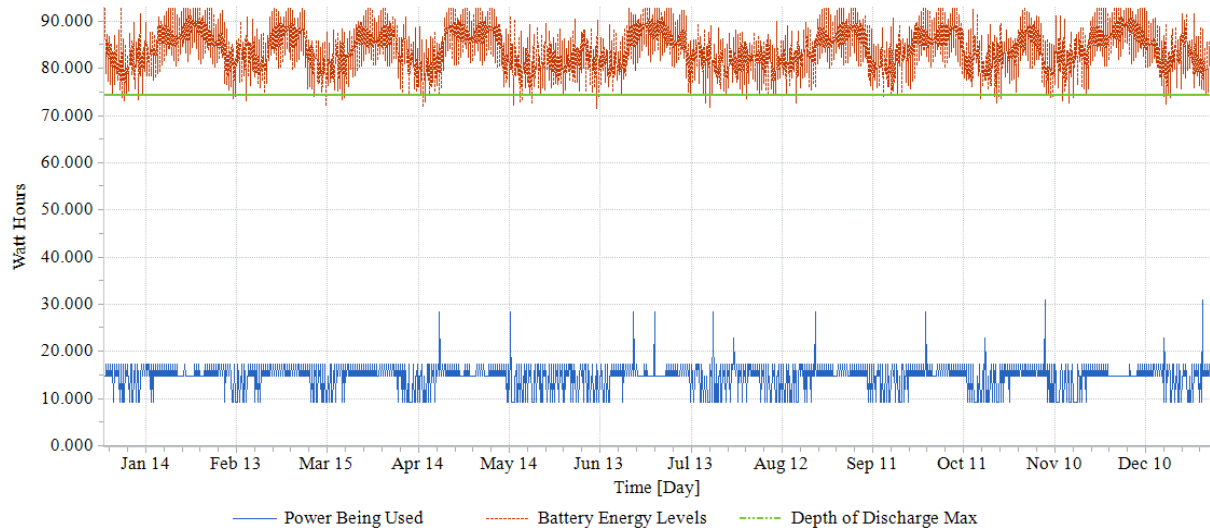
Figure 25: Dual single deployable panels/ double battery pack with sun tracking over one year

The payload availability for this configuration, given in Table 23, has decreased a small amount from the double deployable panel/double battery pack orbiting in LVLH (Table 22).

Table 23: Payload Availability for Single Array/Double Battery with Sun Tracking

Payload	Payload Availability
VT	81.36 %
UIUC	86.18 %

It is clear that the payload operation time in this configuration is reduced due to insufficient power generation due to the single deployable panels. Therefore, in order to reach maximum payload availability, additional solar panels are needed. For the final configuration, LAICE-F was modeled with double deployable solar panels and a double battery pack with sun tracking, which is shown in Figure 26. In the favorable power seasons, the battery is able to recharge completely before LAICE-F enters eclipse, as seen in previous configurations, and the excess power from the panels is shunted away from the batteries. This is not a concern for this configuration, as the battery can provide enough energy during eclipse.
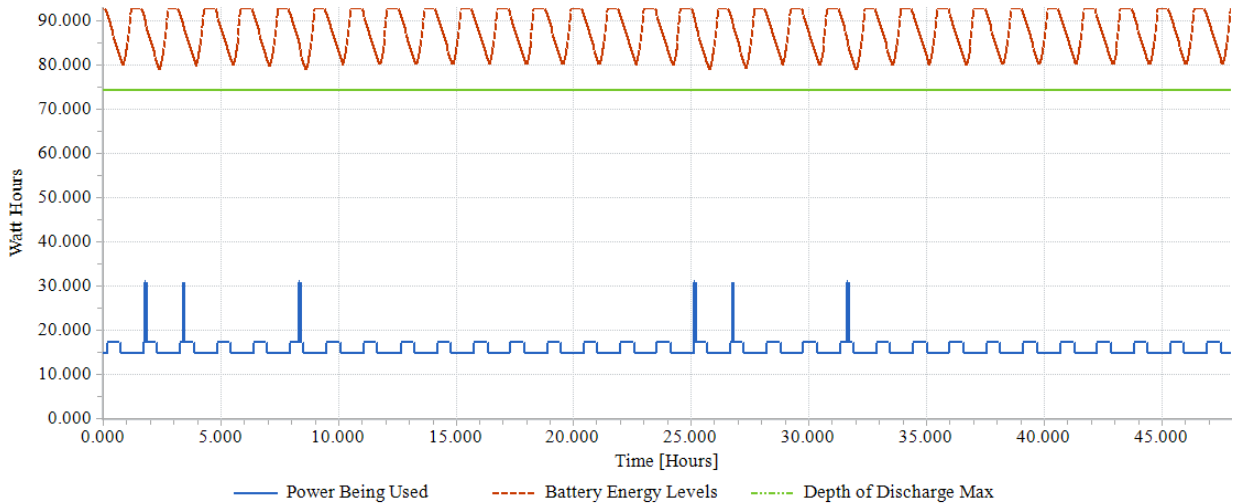
Figure 26: Double deployable arrays/double battery pack with sun tracking

When the energy profile is modeled over one year, it shows LAICE-F is able to maintain nominal battery charging and payload operations (Figure 27), even in the previously challenging dead zones periods.
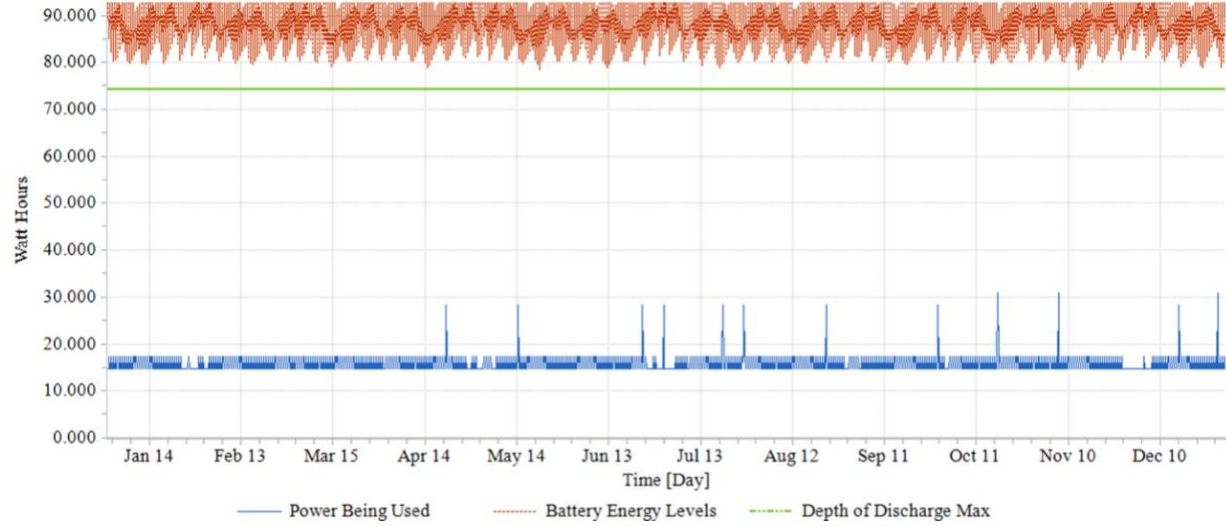
Figure 27: Double deployable panel/double battery pack with sun tracking over one year

Using double deployable solar arrays in addition to a double battery pack finally allows for LAICE-F to have continuous payload operations year round with 100% payload availability (Table 24). The battery also stays well above the acceptable depth of discharge limit for a 2-year mission lifetime.

Table 24: Payload available for double deployable solar panels and double battery pack

Payload	Payload Availability
VT	100 %
UIUC	100 %

In summary, in order to reach the desired 100% payload availability for both UIUC and VT, LAICE-F requires a double deployable solar array configuration with sun tracking and a

double battery pack. This provides acceptable power margins and limits the DOD while maximizing science return. The relevant values are listed in Table 25.

Table 25: Summary of power system parameters

Item	Value
2 X 2 Deployable solar array configuration energy generation (with solar tracking)	47.75 WHrs
Nominal sun tracking solar array power margin	31.98 %
Battery 8 cell capacity	92.72 WHrs
Max battery DOD	16.01%

CHAPTER FIVE: ATTITUDE DETERMINATION AND CONTROL AND CONFIGURATION

In order to determine the necessary attitude determination and control system (ADCS) components for this mission, the relevant requirements for LAICE-F were reviewed. The following table (Table 26) provides a list of the requirements for both the observatory and the payloads that pertain to the ADCS.

Table 26: ADCS requirements

ADCS Performance Requirements		
ADCS-1	**The Observatory shall control the attitude in three axes with an accuracy of ≤ 10° RMS in each axis.**	*The payload instrument sensor pointing vector is maintained on target to within a 10° cone.*
ADCS-2	**The Observatory shall provide pointing knowledge in three axes with an accuracy of ≤ 5° RMS in each axis.**	*The payload instrument sensor pointing vector is known to within a 5° cone.*
PHO-3	**The Photometers shall be aligned to nadir ±10°.**	*This requirement feeds into the ADCS system.*
PHO-4	**The Photometers shall be kept pointed ≥23° away from the sun.**	*This requirement eliminates any first reflection, as sunlight will damage photometers. Only available when ADCS is active.*

The first two requirements listed pertain to the hardware of the system, while the last two concern the software written for the pointing scheme. The architecture of the ADCS, shown in Figure 28, illustrates how the hardware, software, and inputs interact with each other, as well as distinguishing between the determination and the control sections of the subsystem.
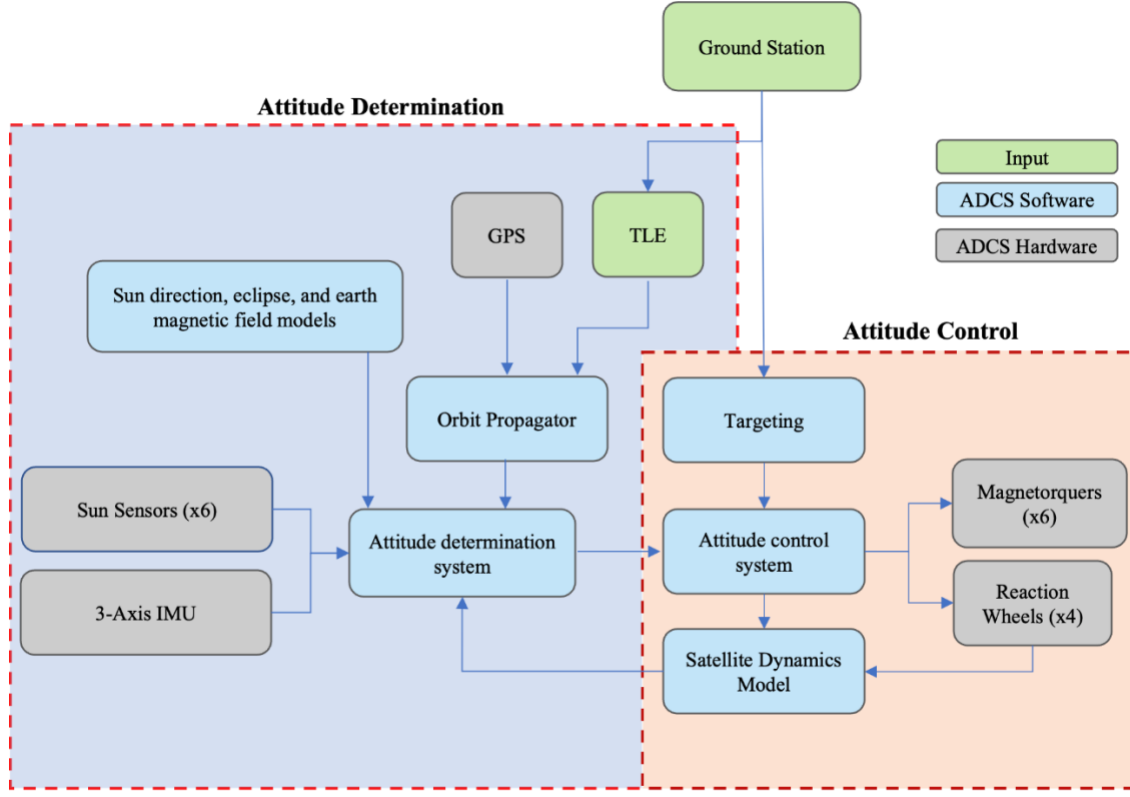
Figure 28: ADCS architecture

The hardware of the attitude determination consists of an inertial measurement unit (IMU), six sun sensors, and a GPS antenna and receiver. A sun sensor is placed on each body face of LAICE-F to provide information on where the sun is in relation to the spacecraft. The IMU provides relative attitude knowledge using three gyroscopes to measure angular rates and three accelerometers to measure linear acceleration in each axes. The specific IMU used in this analysis includes three inclinometers [14]. Data from the IMU combined with the GPS information allows the correct attitude and location of LAICE-F to be known. The GPS includes an antenna and a receiver to transmit and receive information from GPS satellites to provide orbital position initialization knowledge.

The attitude control is provided by six magnetorquers and four reaction wheels. Data are received by the flight computer from the attitude determination system of LAICE-F's current

43

orientation and if a change is desirable, a command is sent to the reaction wheels to orient the satellite to the correct attitude. Three reaction wheels are aligned with the body axes of LAICE-F, while the fourth is at an angle to provide redundancy should a wheel fail. The reaction wheels are used for pointing control while the magnetorquers are used for wheel momentum management when the reaction wheels near saturation. When this occurs, the magnetorquers are used to desaturate in a momentum management maneuver.

Two important values regarding the accuracy of the ACDS is the absolute pointing error (APE) and the absolute knowledge error (AKE). The APE is defined as the instantaneous value of the pointing error at a given time, while the AKE is the instantaneous value of the knowledge error at a given time. These values need to meet the requirements for the ADCS system given in Table 26. The IMU chosen for this mission is able to provide the following error values in Table 27, which allows the requirements to be met.

Table 27: Error for ADCS using IMU

	AKE in Sunlight (1 sigma)	AKE in eclipse (1 sigma)	APE in sunlight (1 sigma)	APE in eclipse (1 sigma)
Coarse determination using IMU	1.25	2.4	1.35	2.55

The ADCS is capable of meeting payload pointing requirements of $\pm 10°$. The analysis is to be provided by NanoAvionics as part of CDR effort.

Bus Configuration and Mass Budget

After components were selected, the physical layout of the bus was configured to confirm design feasibility. The components were integrated into the CAD model of the bus structure

along with the payloads to assess configuration options. After feasibility was confirmed, mass and volume budgets were made.

To create the CAD model, the payload assembly files were converted to NX parts and updated. The component files provided by manufacturers were converted to NX parts and then constructed into subassemblies, which can expand to display primary components. The external view of LAICE-F in science collection mode is shown in Figure 29.
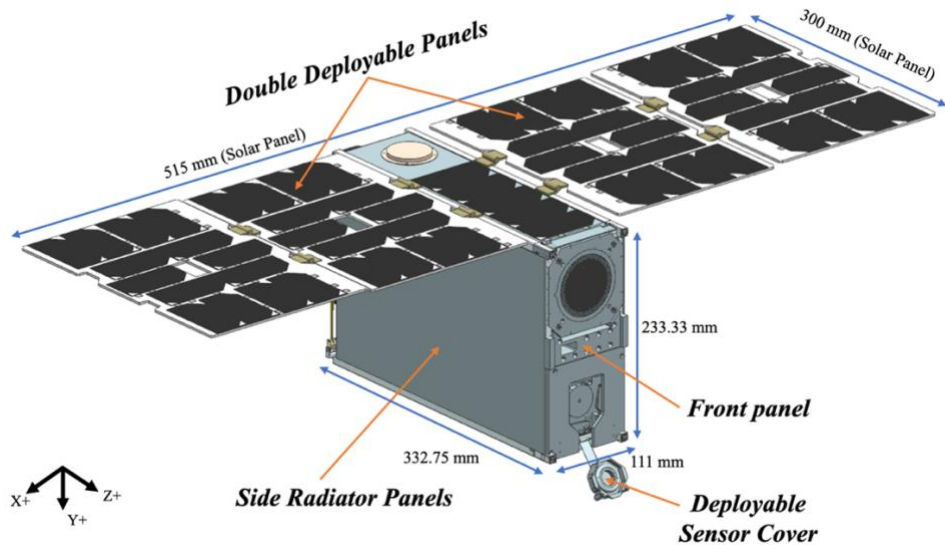
Figure 29: External view of LAICE-F with solar panels and cover deployed

Approximately 4U of LAICE-F is occupied by the scientific instruments. The batteries are located in additional storage capsules, "tuna cans", at the back end of the satellite. The space above the photometers and behind the VT payload houses the reaction wheels, the IMU, the service stack, the magnetorquers, and the S-band transceiver. The UHF splitter antennas are located along the rear frame edge. The GPS patch antenna is placed on the anti-nadir face alongside the solar cells. The internal view with the frame is shown in Figure 30, with each component labeled.
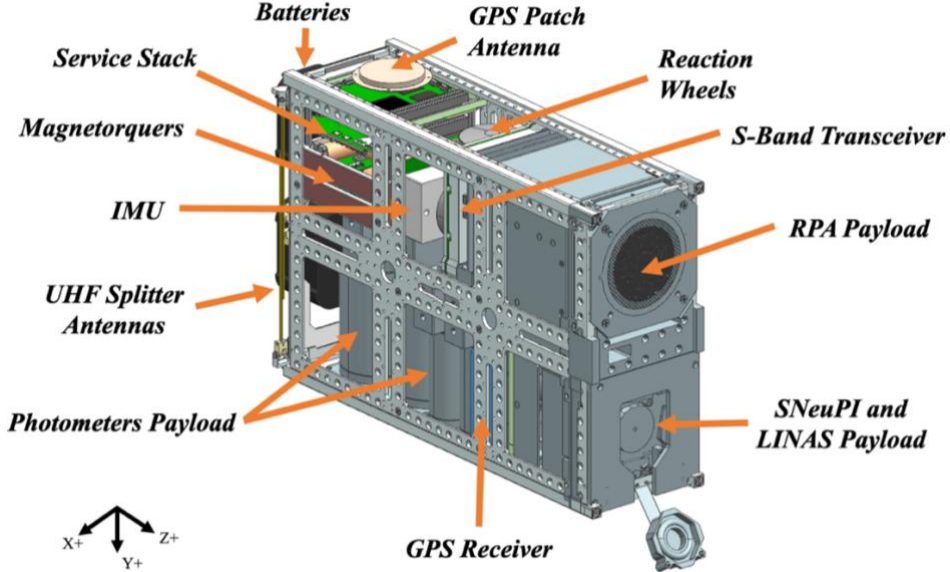
Figure 30: Internal view of LAICE-F with components labeled

The photometers were rearranged to accommodate overhead bus components. This configuration shows the two larger photomultiplier tubes placed next to each other with the five smaller ones together in the middle of the frame. The S-band patch antenna sits on the anti-nadir side of LAICE-F by the VT payload suite. Figure 31, seen below, shows the internal side view without the frame, with the GPS receiver and batteries clearly visible, and the service stack boards individually labeled.
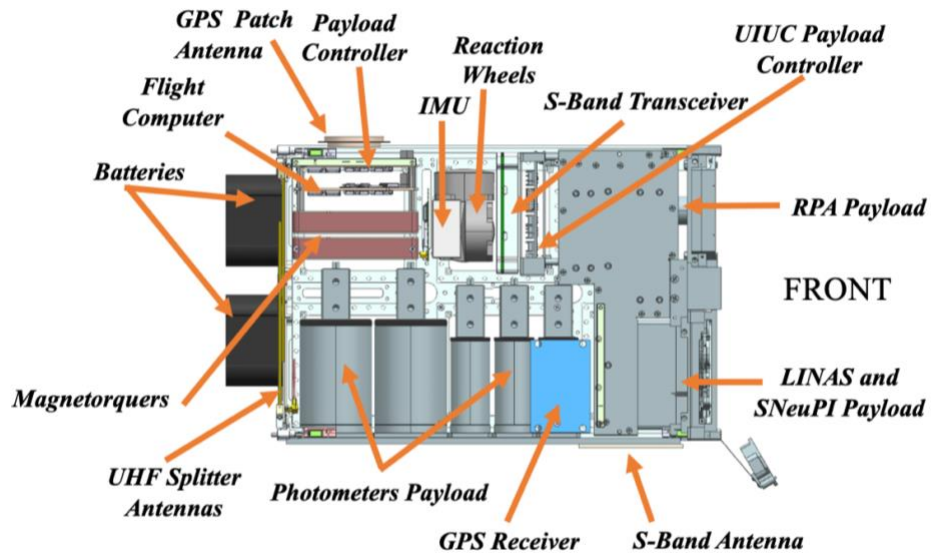
Figure 31: Internal side view of LAICE-F with external frame removed

Figure 32 shows the internal view, with the nadir face visible to show the placement of the photometers, allowing the GPS transceiver to fit beside the frontmost tube.
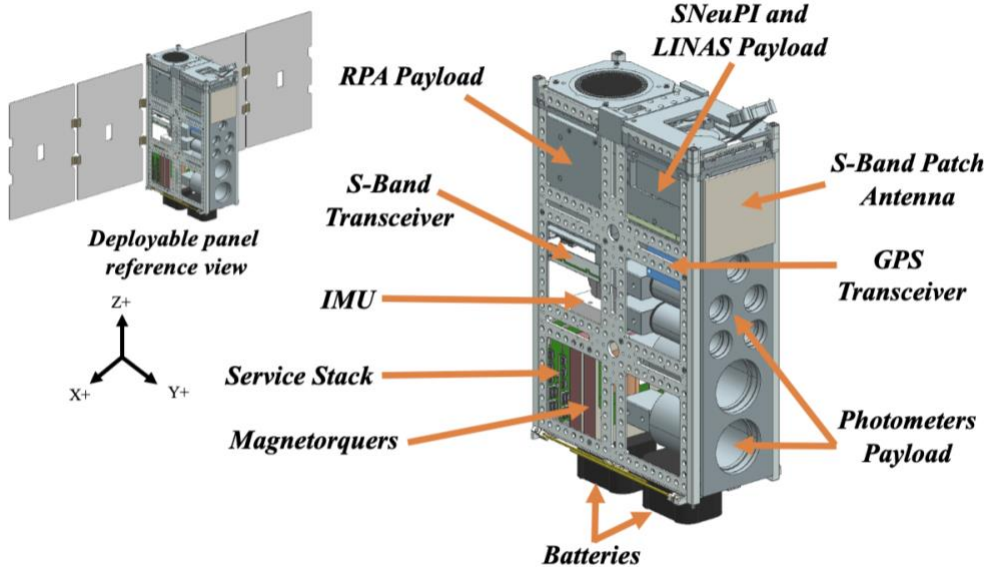
Figure 32: Internal view of LAICE-F with components labeled

Finally, the front and back view of LAICE-F are shown in Figure 33. The VT payloads are shown in the ram direction, and the batteries in the tuna cans are shown on the back of LAICE-F, with the GPS patch antenna located in the anti-nadir direction.
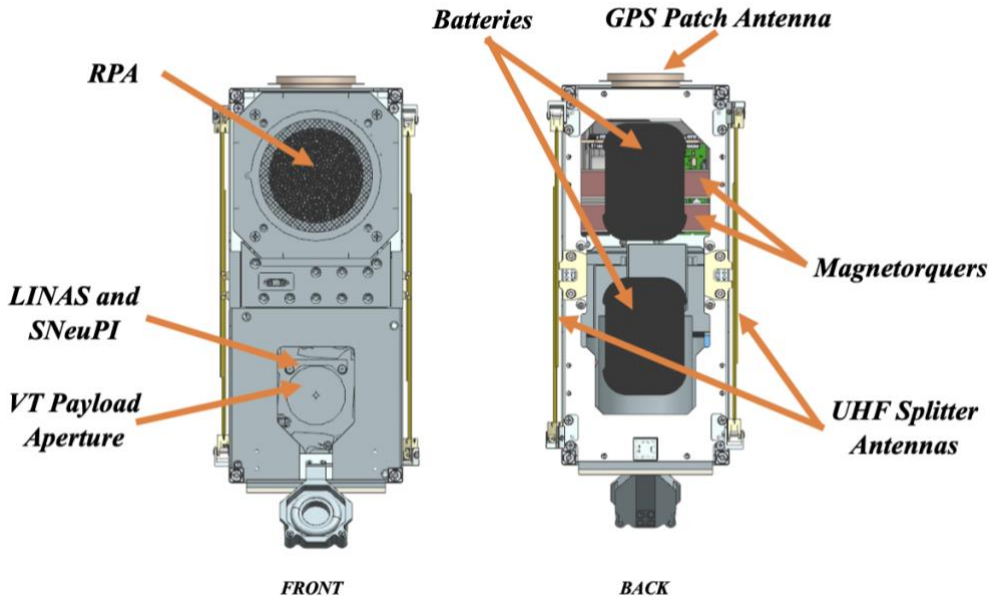
Figure 33: Front and back view of LAICE-F showing components

Mass Budgets

To complete the mass budget for LAICE-F, a table of the mass of each physical component, the margin applied, and the total margined mass for that component was made, shown below in Table 28. With these estimates, the total margined mass estimate for LAICE-F was calculated. The mass of each component was found from specification sheets for COTS parts and provided from NanoAvionics for their components.

Table 28: LAICE-F complete mass budget with margins applied

Component	Subsystem	Manufacturer	Mass (g)	Qnt	Unmargined Mass (g)	Margin (%)	Margin Mass	Total Mass
6U Frame	Structure	NanoAvionics	725.0	1	725	5%	36.3	761.3
(1x3)U Bus Panel	Structure	NanoAvionics	136.66	1	136.66	5%	6.8	143.49
(1x3)U Bus Payload Panel	Structure	NanoAvionics	114.74	1	114.74	20%	22.9	137.69
(1x2)U Bus Panel	Structure	NanoAvionics	95.83	1	95.83	5%	4.8	100.62
(1x2)U Bus Payload Panel	Structure	NanoAvionics	70.14	1	70.14	20%	14.0	84.16
(2x3)U Radiator Panel	Structure	NanoAvionics	419.26	2	838.52	5%	41.9	880.45
Reaction Wheel Configuration Plate	Structure	NanoAvionics	117.0	1	117	5%	5.9	122.85
Deployable Solar Panel	Structure	NanoAvionics	235.0	2	470	5%	23.5	493.5
Solar Cells	Power	Azur Space	2.6	61	158.6	5%	7.93	166.53
EPS	Power	NanoAvionics	190.0	1	190	5%	9.5	199.5
Batteries	Power	NanoAvionics	60.0	8	480	5%	24.0	504
Flight Computer	Avionics	NanoAvionics	102.5	1	102.5	5%	5.1	107.63
Payload Controller	Avionics	NanoAvionics	110.0	1	110	5%	5.5	115.5
Sun Sensors	ADCS	Solar MEMS Technologies	4	6	24	5%	1.2	25.2

Table 28: LAICE-F complete mass budget with margins applied (cont.)

Component	Subsystem	Manufacturer	Mass (g)	Qnt	Unmargined Mass (g)	Margin (%)	Margin Mass	Total Mass
IMU	ADCS	Safran	55.0	1	55	5%	2.75	57.75
GPS Receiver	ADCS	Sky Fox Lab	24	1	24	5%	1.2	25.2
GPS Antenna	ADCS	Tallysman	100.0	1	100	5%	5.0	105.0
Magnetorquer	ADCS	NanoAvionics	31.0	6	186	5%	9.3	195.3
Reaction Wheels	ADCS	NanoAvionics	137.0	4	548	5%	27.4	575.4
S-band Transceiver	RF	SatLab	190.0	1	190	5%	9.5	199.5
S-band Dual Patch Antenna	RF	IQ Wireless	49.0	1	49	5%	2.5	51.45
UHF Radio	RF	NanoAvionics	7.5	1	7.5	5%	0.4	7.88
UHF Splitter	RF	NanoAvionics	57.0	1	57	5%	2.9	59.85
Photometer Payload	Payload	UIUC	1563.9	1	1563.9	0%	0	1563.9
VT Payload	Payload	VT	3200	1	3200	0%	0	3200
Cabling / Harnesses	Structure	NanoAvionics	455.18	-	455.18	20%	91.0	546.23
Secondary Structural Components	Structure	NanoAvionics	1137.97	-	1137.97	20%	227.6	1,365.56
Totals					**11,206.5**		**588.8**	**11,795.3**

Bus components were selected from the NanoAvionics 6U bus solution, excluding custom brackets, and mounting hardware. NanoAvionics can provide solutions for custom frames, panel aperture, and mounting brackets. Mass margin is applied at the component level, with the percent applied corresponding to the type of component, and is listed below in Table 29. According to AIAA mass growth allowance standards, the mass margin applied depends on the design maturity for components. The margin applied for vendor supplied components is 5%, while 20% is applied to custom components [15]. Since the payloads are existing flight

hardware, they were each measured in the lab, which allows for no margin with regards to their total mass. The harness and secondary structures margin is an overall percentage of the bus mass.

Table 29: Component mass margins

Applied Mass Margins	
Vendor supplied	5%
Custom component	20%
Payload (measured)	0%
Harness (percentage of bus mass)	10%
Secondary structures (percentage of bus mass)	10%

With these mass margins applied, the breakdown of the final mass budget for LAICE-F is given in Table 30, comparing the estimated margined mass to the allowed mass of a 6U CubeSat.

Table 30: Final LAICE-F mass budget

Breakdown	Mass (g)
Total margined mass	11,795.3
Allowed mass	12,000.0
Remaining mass	204.7
Remaining mass %	1.7%
Mass from margin	588.8
Mass from margin %	4.91%
Total mass margin	6.61%

A total mass margin of 6.61% presents a significant challenge for mass management at PDR going forward into detailed design, especially considering the margin is expected to decrease as hardware is delivered and final mass measurements are obtained. Figure 34 shows how the mass margin decreases over the mission design timeline [16].
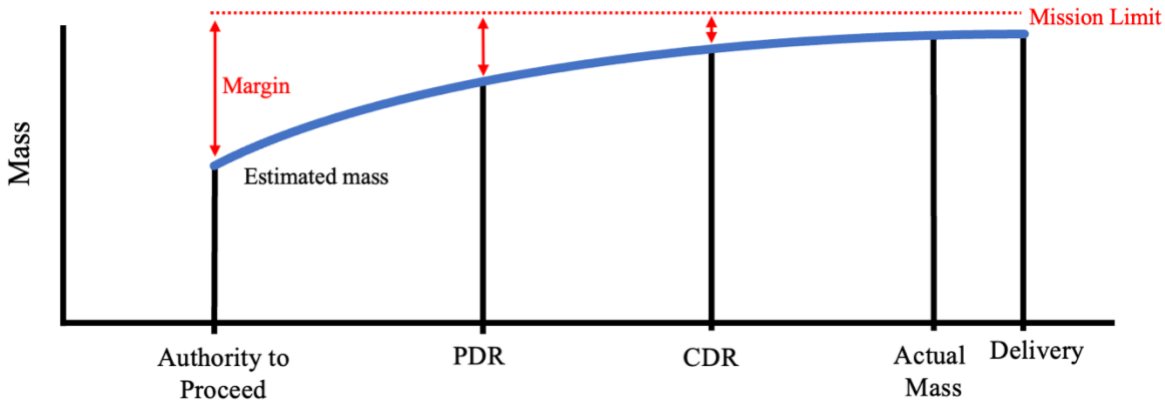
Figure 34: Mass growth over mission timeline

Volume Budget

Similarly, to how the mass budget was made, a volume budget was composed for LAICE-F. The volume for each component was tabulated and summed to determine the estimated volume for LAICE-F. No margins were applied to the volume estimates. The complete table is given below in Table 31.

Table 31: LAICE-F complete volume budget

Component	Manufacturer	Subsystem	Volume [cm³/unit]	Qnt	Total Volume [cm³]	Information Source
Flight Computer	NanoAvionics	Avionics	146.132	1	146.132	Spec Sheet
Payload Controller	NanoAvionics	Avionics	146.132	1	146.132	Spec Sheet
EPS Board	NanoAvionics	Power	104.063	3	312.192	Spec Sheet
Batteries	NanoAvionics	Power	16.324	8	130.593	Spec Sheet
Magnetorquers (each)	NanoAvionics	ADCS	12.847	6	77.082	Spec Sheet
Reaction Wheel	NanoAvionics	ADCS	41.108	4	164.435	Spec Sheet
Reaction Wheel Configuration Plate	NanoAvionics	ADCS	25.668	1	25.668	Spec Sheet
Sun Sensor	Sky Fox Labs	ADCS	2.26	6	13.56	Spec Sheet
GPS Receiver	Sky Fox Labs	ADCS	35.926	1	35.926	Spec Sheet
GPS Antenna	Tallysman	ADCS	139.258	1	19.211	Spec Sheet
IMU [STIM300]	Safran	ADCS	37.179	1	37.179	Spec Sheet
S-Band Transceiver	SatLab	RF	137.547	1	137.547	Spec Sheet
S-Band Patch Antenna	IQ Wireless	RF	40.500	1	40.500	Spec Sheet
Secondary Structural Components	Misc.	Structure	123.959	-	123.959	Estimate
Cabling / Harnesses	Misc.	Misc.	123.959	-	123.959	Estimate
RPA	Virginia Tech	Payload	1282.041	1	1282.041	Hardware
LINAS and SNeuPI	Virginia Tech	Payload	2414.420	1	2414.420	Hardware
Photometers	UIUC	Payload	2178.450	1	2178.450	Hardware
Totals					**7408.99**	

Bus components are from the current NanoAvionics 6U bus specification, excluding custom brackets and mounting hardware. Each payload was measured to obtain an accurate volume. The volume budget is given in Table 32.

Table 32: Final LAICE-F volume budget

Breakdown	Volume (cm^3)
Used Volume	7408.99
Allowed Volume	8618.10
Remaining Volume	1209.11
Remaining Volume %	14.03%

CHAPTER SIX: DATA AND COMMUNICATIONS ANALYSIS

The purpose of the communications system is to provide an interface between LAICE-F and the ground station. This allows LAICE-F to send payload data and telemetry to the ground and the ground station to send commands to the satellite. The data rates for the payloads and bus are given in Table 33. The data rates for the payloads were obtained based on the required data fields document and information from the PIs.

Table 33: Downlink data budget

Data	Value
Bus Total	384 bytes per second
VT Payload	338 bytes per second
UIUC Payload (33% Duty Cycle)	21 bytes per second
Overhead (25%)	~183 bytes per second
Total Bytes Per Second	~912 bytes per second

Since the photometers are only collecting data during eclipse, 912 bytes per second is the maximum data rate that LAICE-F will generate throughout its orbit. The components of the communications system were chosen such that the link budget for LAICE-F closed (i.e. the components are capable of sending the data LAICE-F generates to the ground as well as receive commands uplinked).

Both UHF and S-band radios were considered for data relay, and the data transmission rates were compared, as seen in Table 34. Assuming each payload was able to operate for the desired duty cycle, the percent of data each radio could transmitted was calculated.

Table 34: Uplink/downlink requirements

Radio	Data Rate	Percentage of command data that can be uplinked	Percentage of data that can be downlinked
UHF	1.2 KBps	100%	1.4%
S-Band	3.3 MBps	100%	100%

Due to the low bandwidth of the UHF radio, it is woefully inadequate for the amount of data LAICE-F needs to downlink. However, it is sufficient for command uplink. The S-band radio provides required bandwidth for both downlink and uplink but presents concerns regarding ground station selection.

As the LASSI ground station currently only supports UHF communications, other options need to be explored. The ground station selection will need to be evaluated at CDR.

In order to complete the link budget, the following components were selected. The Satlab SRS-3 is a low power S-band transceiver made for CubeSats, and only requires passive external antennas [17]. The key parameters are outlined in Table 35 below.

Table 35: Description and specifications of S-Band transceiver

S-band Transceiver		
Model Number	SATLAB SRS3	
Description	Full-duplex, S-band transceiver	
Dimensions	87 x 93 x 17 mm	
Mass	0.190 kg	
Full-duplex Transmit and Receive Power	5.0 W	
Power Consumption (Idle)	550 mW	
Supplied Voltage	5 - 40 V	
Frequency Range	Tx: 2200-2290 MHz Rx: 2025-2110 MHz	
Transmit Power	20-30 dBm	

The S-band patch antenna made by IQ Spacecom is a circular polarized, flight-proven antenna designed for CubeSats [18]. Its low mass and volume allow it to be placed on the exterior anti-nadir face, as shown in Chapter Five. The specifications for this antenna are given below in Table 36.

Table 36: S-Band patch antenna parameters

S-Band Antenna		
Model Number	IQ S-Band Patch	
Description	IQ Spacecom Dual Patch for S-Band TX and RX	
Dimensions	70 x 70 mm	
Mass	0.049 kg	
Frequency Range	2,100-2,500 MHz	
Antenna Gain	6 dBi	
Bandwidth	50 MHz	

The SAT2RF1-1D made by NanoAvionics provides a low power solution for a CubeSat UHF transceiver [19]. The key parameters are given below in Table 37.

Table 37: Description and specifications for UHF transceiver

UHF Transceiver		
Model Number	SAT2RF1-1D	
Description	Half-duplex UHF transceiver	
Dimensions	33 x 47 x 6 mm	
Mass	0.0075 kg	
Full-duplex Transmit and Receive Power	3.0 W	
Supplied Voltage	3.3 V	
Frequency Range	395-440 MHz	
Transmit Power	<34 dBm	

With the components selected, a LASSI link budget spreadsheet tool was used to evaluate the link margins for the communications system. For both uplink and downlink communications, a QPSK modulation scheme is used. The budget for the UHF command uplink provides sufficient uplink margins, as shown in Table 38.

Table 38: Link budget for command uplink

Parameter	Value
Data Rate	9.6 kbps
Transmit Power	200 W (23dBW)
Frequency	2110 MHz
Modulation	QPSK
Link Margin	19.8 dB

Similarly, the S-band link budget supports sufficient downlink margins, shown in Table 39.

Table 39: Link budget for data downlink

Parameter	Value
Data Rate	210 kbps
Transmit Power	1W (30 dBm)
Frequency	2200 MHz
Modulation	QPSK
Link Margin	10.4 dB

Since the S-band radio can only transmit data when it is in range of the ground station, LAICE-F must provide on-board storage for data to be stored before it can be downlinked. The payload controller is able to store up to 128 MB of data from the payloads, which fills at the rate specified in Table 33 for each component [11]. As mentioned previously, Free Flyer was used to model contact between LAICE-F and a ground station located in Urbana-Champaign. When LAICE-F is in view of the ground station, the stored data is downlinked, and space is freed up on the payload controller. The profile of the onboard storage availability over the course of one month is shown below in Figure 35.
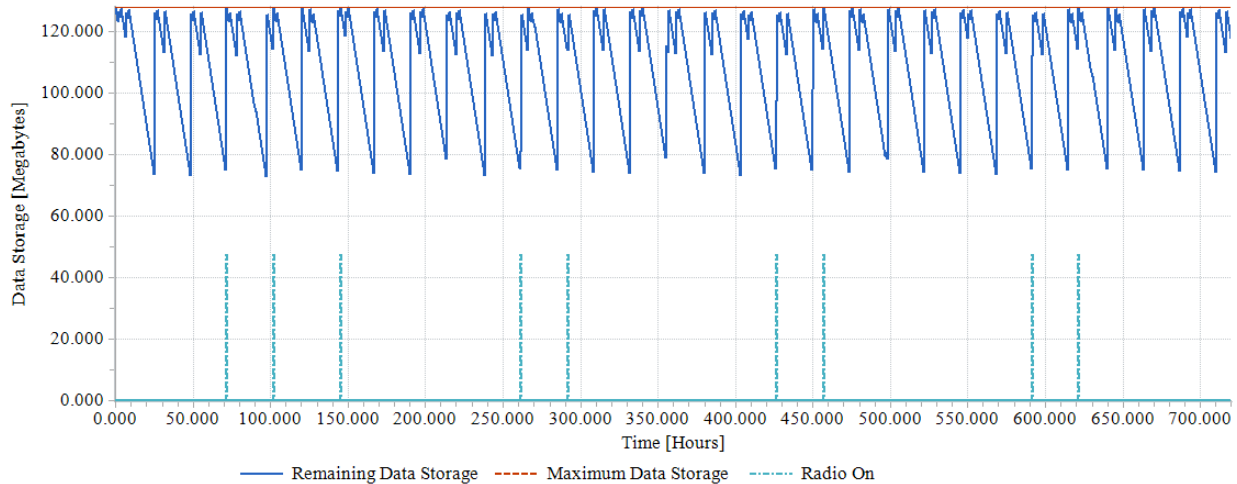
Figure 35: Onboard storage availability and downlink passes (one month)

Each vertical line on the bottom half of the X axis (turquoise) shows a major communications pass, and the curve on the top of the X axis (dark blue) shows the increase of storage available as the satellite completes the pass. As LAICE-F downlinks data to the ground, it frees up storage onboard. As the length of the communication passes decreases, not all of the stored data is able to be downlinked during the pass. The maximum delay in downlinking all the stored data can been seen in Figure 36.

59
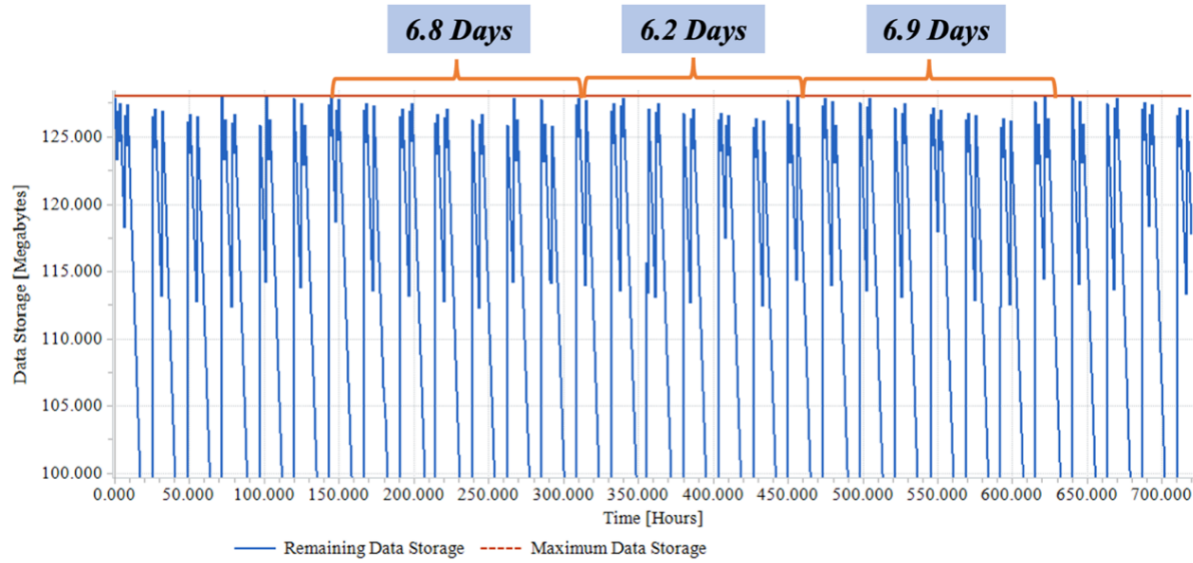
Figure 36: Maximum delay for emptying on-board storage

The data that builds up during these delays is stored onboard using the payload controller. Using an S-band system for data downlink and a UHF for command uplink, LAICE-F satisfies the payload operations and data retrieval mission requirements.

CHAPTER SEVEN: THERMAL ANALYSIS

The objective for the thermal analysis was to evaluate the thermal management by LAICE-F by identifying internal and external heat loads and modeling the thermal subsystem architecture. This was achieved by creating a model in Siemens NX Space Systems Thermal for thermal simulation and analysis. The model was originally built by another LASSI graduate student, Michelle Zosky, for another satellite project. This program allowed the team to specify orbital parameters and spacecraft attitude and is able to simulate a fully coupled conduction and external radiation heat transfer paths [20]. Each simulation was run for ten orbits, and computed temperatures across all elements, total heat loads, total heat flux, radiation, and albedo. The model for the thermal system is shown in Figure 37.
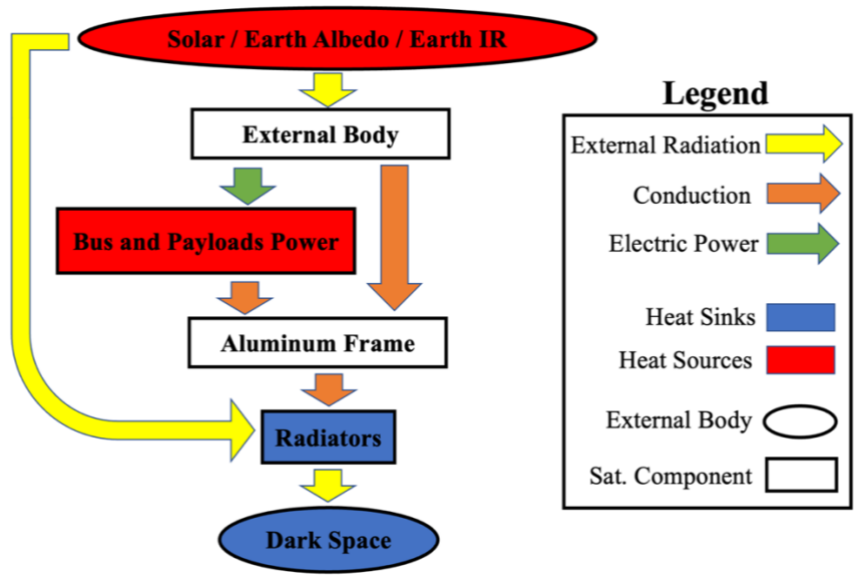

Figure 37: Thermal energy flow chart

The radiator shown in this model is an external panel of LAICE-F that acts as a radiator. A simplified model was made by applying a 2D mesh with appropriate thickness to individual parts using automatic element sizing. Surface-to-surface contacts were assigned to each part to

show conductance, with perfect contact used between conductive interfaces. Heat loads and temperature constraints were applied to the model, using the power consumption from the components and payload boards. The values are shown in Table 40. The harness connecting the payloads to the electronics were not considered in this simplified model.

Table 40: Internal heat loads applied

Internal Heat Loads Applied	Value (W)
VT payload	8.65
UIUC payload	0.90
Bus subsystem components	6.01

Each heat load was modeled as 12 individual points across the satellite frame, and the total head loads are distributed across the mounting points as seen in Figure 38.
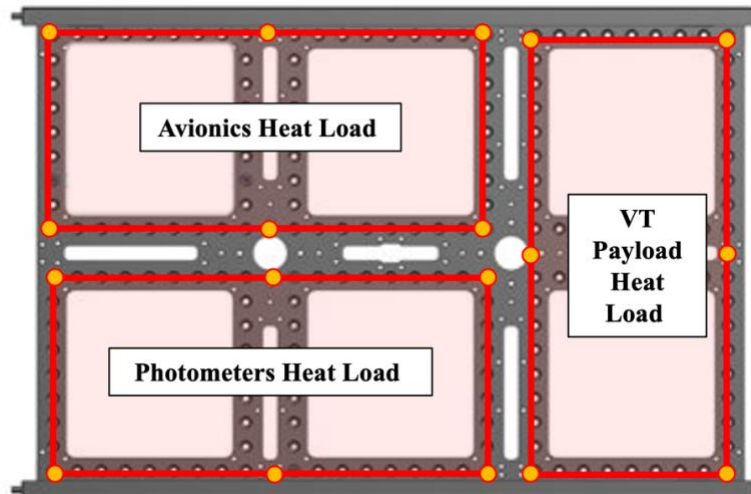
Figure 38: Heat load modeling points

Orbital heating was included as a simulation object using mission-specific parameters and 12 calculation positions per orbit. Exterior surfaces were assigned to receive external radiation using low, Hemicube-based view factor calculations, with deterministic ray-tracing,

and no element subdivision. Reduced mesh resolution was used for the radiation view factor calculations to reduce computation time. The NX model, seen in Figure 39, is configured with the LVLH attitude nominally anticipated during mission operations.
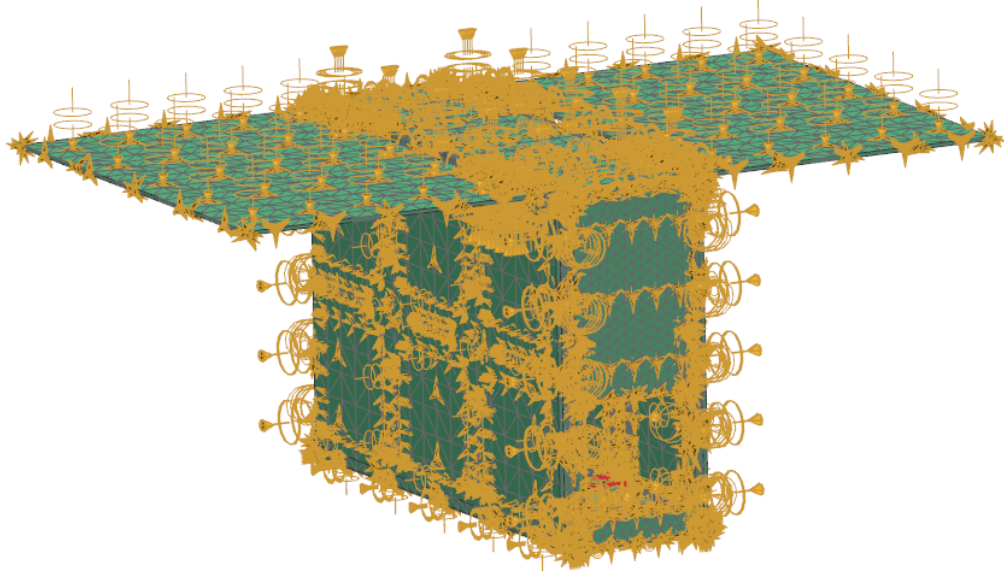
Figure 39: Meshed and loaded NX thermal model [20]

To obtain a comprehensive understanding of the temperatures LAICE-F is expected to experience, the model was analyzed at both deployment altitude and EOL altitudes throughout the year on the equinoxes and solstices, as shown in Table 41.

Table 41: Analyzed orbital parameters

Orbit Parameters	Value
Altitude	425 km 350 km
Inclination	51.6°
GMT Dates Assessed	March 21 June 21 September 21 December 21

The variation in temperature across the external radiator panel is shown in Figure 40 for December 21, at 425 km altitude in daylight, with LAICE-F in LVLH orientation. The minimum and maximum temperatures it experiences are listed in Table 42. This shows the total temperature variation across the panel is less than 1° C.
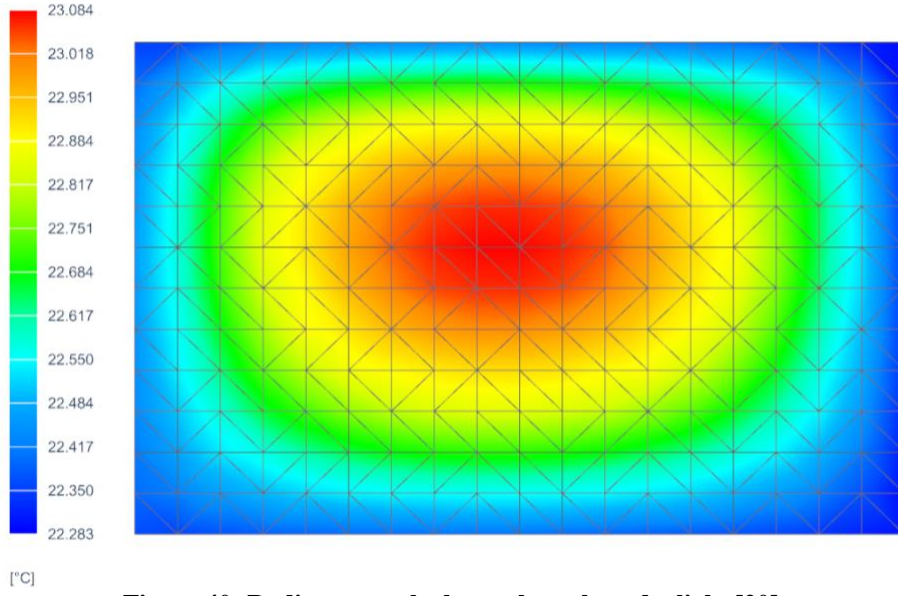
Figure 40: Radiator panels thermal results – daylight [20]

The maximum temperature the panel experiences is slightly off-center, skewed towards the higher heat load from the bus components instead of the photometers. The temperature drops off towards the edges of the panel. Table 42 shows the maximum and minimum temperatures LAICE-F sees in daylight on December 21st.

Table 42: Maximum and minimum temperatures for Dec. 21 at 425 km in sunlight

Radiator Panels Temperature December 21st, 425 km, Sunlight	
Max Temperature	23.08° C
Min Temperature	22.28° C

Next, the variation in temperature across the radiator panel for LAICE-F in eclipse is shown in Figure 41. This is for December 21, at 425 km altitude in eclipse, in LVLH orientation.
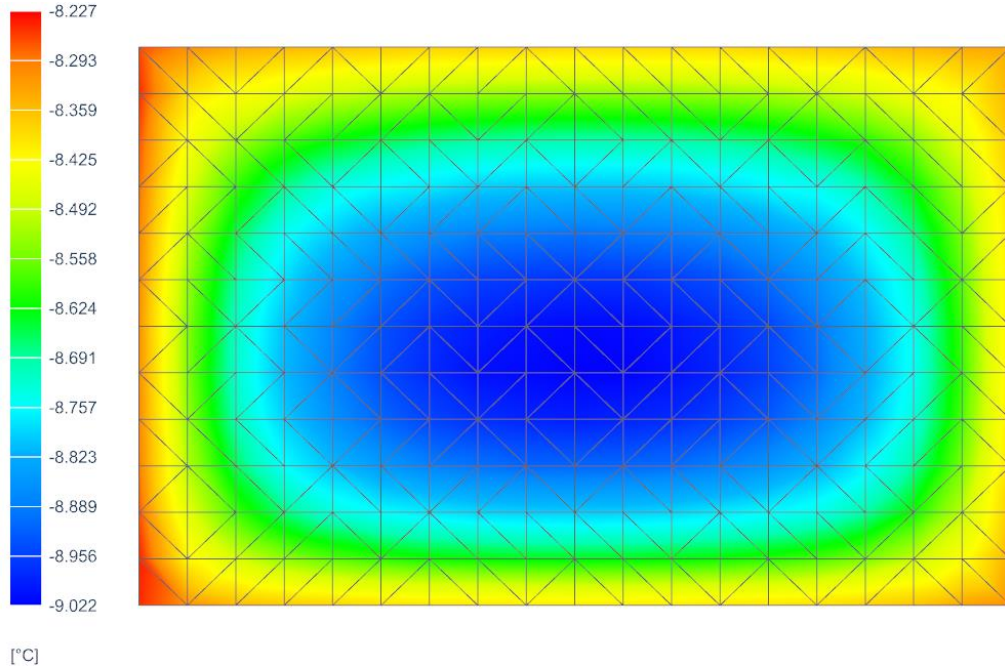
Figure 41: Radiator panels thermal results – cold [20]

Again, a lower temperature occurs closer to the photometers, and the total temperature variation across the panel is again less than 1° C. Table 43 shows the minimum and maximum temperatures the panels experience in eclipse.

Table 43: Temperatures of radiator panel for Dec 21 at 425 km in eclipse

Radiator Panels Temperature December 21st, 425 km, Eclipse	
Max Temperature	-8.22°C
Min Temperature	-9.02°C

While the panel temperature varies by less than 1° C during each part of the orbit, the variation in temperature between daylight and eclipse is more extreme, going from 23° C to -9°

C. The temperature variation over 10 orbits at 425 km starting December 21st can be seen in Figure 42.
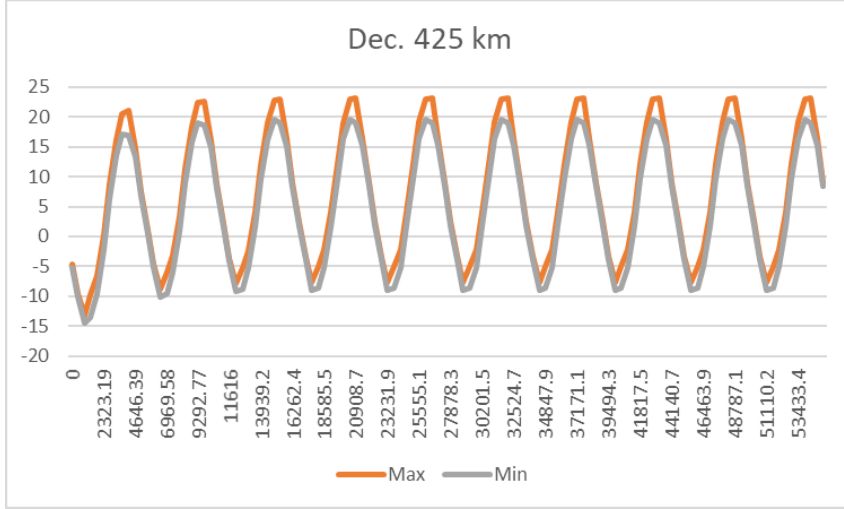
Figure 42: Radiator panels thermal result over 10 orbits for Dec 21 at 425 km

This shows that the panel temperature varies across the orbit by ~ 32° C, which is within the operational bounds of the bus hardware specifications [19]. The summary of temperature variations across daylight and eclipse and deployment altitude and EOL altitude is shown below in Table 44. The main take away is that the altitude and time of year have minimal effect on the thermal configuration of the satellite.

Table 44: Summary of thermal results

Altitude	350 km		425 km	
Month	Max °C	Min °C	Max °C	Min °C
March	15.75	-14.15	15.15	-14.76
June	19.67	-11.07	19.14	-11.60
September	14.86	-14.62	14.25	-15.25
December	23.61	-8.38	23.08	-9.02

CHAPTER EIGHT: RISKS AND CONCLUSION

Risks

Over the course of completing this preliminary design review, six risks have been

identified that could adversely impact the mission if realized. Mitigation plans for each risk have

been devised to minimize the risk. After identifying each risk, the probability that it will occur

(likelihood) versus the severity of the consequence was listed. The range for each value is 1 to 5,

with 5 representing a "very likely to occur" probability and a mission-failure consequence. These

risks and mitigation plans are presented below in Table 45.

Table 45: Risks and corresponding mitigation plans
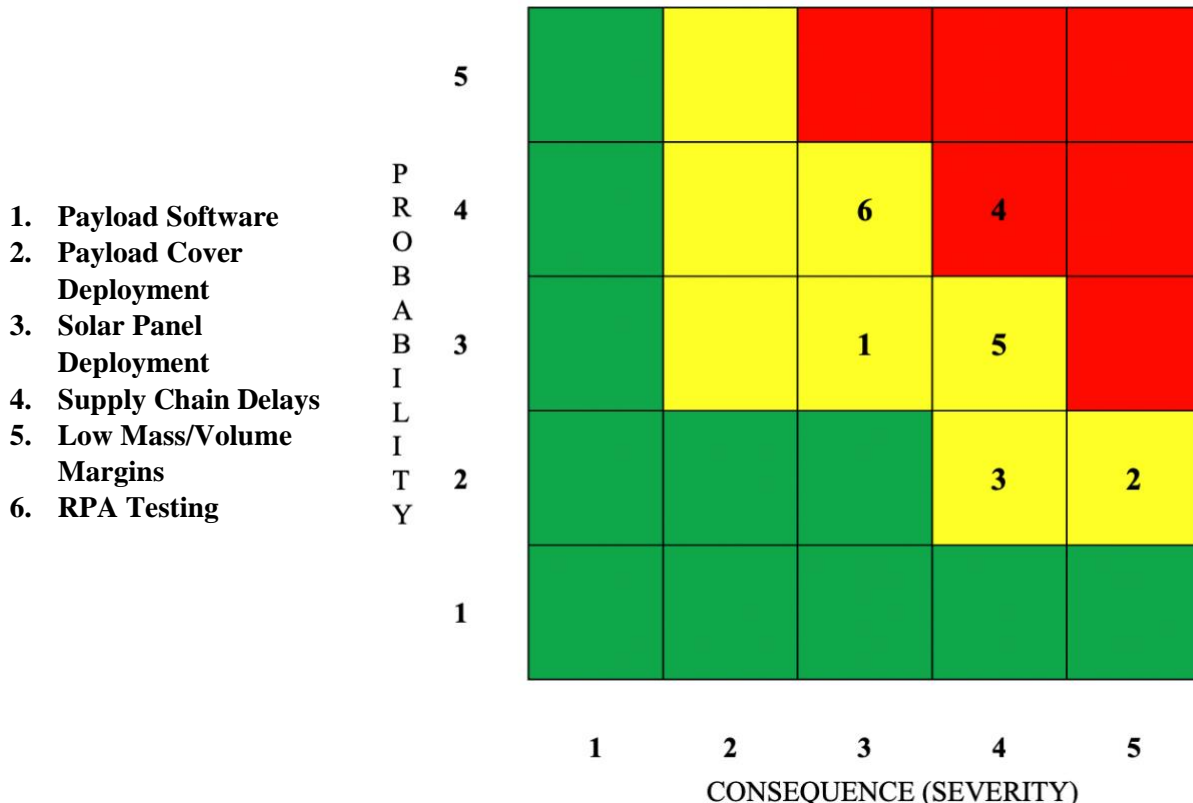
#	Risk	Likelihood	Consequence	Mitigation Plan
1	Given that most of the payloads' flight software was written several years ago, there is a **medium** risk that payload software development for a new payload controller board may present unanticipated challenges and development delays.	3	3	Devote engineering time to assess available code and evaluate work required to port it to new controller board as part of CDR tasks.
2	Given that the LINAS and SNeuPI payloads require a deployable sensor cover, there is a **low** risk that there will be a deployment failure adversely impacting the data collection ability of the payload, leading to a significant mission failure.	2	5	Refurbish any seals and other limited lifetime items prior to final environmental testing.
3	Given that LAICE-F requires more complex double deployable solar panels, there is a **low** risk of a failure to deploy, adversely impacting the power generation and thermal performance of the satellite, leading to a partial mission failure.	2	4	The solar array vendor will be required to demonstrate an array deployment ground test prior to acceptance by the spacecraft.

4	Given that supply chain issues continue in the near term, there is a **high** risk of electronic component supply availability adversely impacting the mission development schedule.	4	4	If available, funding should be reserved for early (at risk) procurement of long lead parts prior to CDR.
5	Given low volume and mass margins at PDR, there is a **medium** risk of exceeding launch deployer capability.	3	4	Careful management of remaining margins should be sufficient to complete development. Some capability descope can reduce mass further with minor impacts to payload operations.
6	Given that the RPA has not been flown in this configuration, it needs to be tested to verify the biased voltages for each grid post environmental testing. This poses a **high** risk for screws coming loose given that the screws will be taken out and replaced post-test.	4	3	Procure waiver from NASA for post-vibration testing for VT payload.

Two of the six risks are identified as high risks. The first, Risk 4, concerns supply availability impacting the mission schedule. The proposed mitigation plan is to set apart funding for early procurement of parts with especially long lead times. The second high risk, Risk 6, is in regard to the RPA and testing the voltages post environmental testing. This requires removing screws from LAICE-F and replacing them, which poses a high risk of screws loosening during launch. To mitigate this risk, a waiver from NASA should be procured for post environmental testing for the RPA. Each risk is plotted graphically below in Table 46.

Table 46: Probability vs. consequence of risks

1. **Payload Software**
2. **Payload Cover Deployment**
3. **Solar Panel Deployment**
4. **Supply Chain Delays**
5. **Low Mass/Volume Margins**
6. **RPA Testing**

Conclusion

This concludes the preliminary design of LAICE-F, a 6U CubeSat mission between UIUC and VT to observe gravity waves in the atmosphere. As the previous design, LAICE, proved incapable of supporting the mission requirements, a redesign of the satellite bus was completed to ensure the mission objectives were met. Flying four payloads and meeting all mission requirements on a 6U CubeSat proved to be a significant design challenge, mainly regarding power availability and volume and mass constraints, as outlined in Chapters Four and Five. For the current design, LAICE-F employs double deployable solar panels with sun tracking and an 8-cell battery pack to meet the mission requirements for 100% payload availability. These changes will be a significant increase in the mission cost.

As efforts continue towards CDR, there are some proposed ideas for power budgeting to assist with cost, and volume and mass limitations. However, these come at the cost of impacting the mission objectives. These options include powering LINAS off once SNeuPI is verified or operating the entire VT suite only while the photometers are operating during eclipse or accepting a reduced payload availability. For a reduced load on the batteries, a constraint of having communications sessions only during daylight could be imposed. Additional analysis to the material presented here is needed to determine the decrease in payload availability and the optimal payload scheduling if LAICE-F used single deployable solar arrays in place of the double deployable arrays, or if an LVLH attitude is maintained throughout the orbit, with no sun tracking scheme used. Evaluating the ADCS performance and verifying mechanical and electrical interfaces between the payloads and subsystems, along with various other items will be completed for a CDR.

The preliminary design of LAICE-F outlined here provides a detailed solution to fly VT and UIUC hardware in the lower atmosphere for atmospheric gravity wave measurements with 100% payload availability. The mission will focus on increasing the current understanding of the generation of gravity waves in the lower atmosphere, mainly by weather systems and local topography. The main goals for LAICE-F are first, to measure airglow brightness in the lower F-region heights, which is accomplished via the UIUC photometers. Second, to take in-situ measurements of ion and neutral density, which is fulfilled by the VT payload suite made up of LINAS, SNeuPI, and the RPA. Finally, the end goal is to correlate the remote and in-situ measurements and create maps of active gravity wave regions. These objectives can be met with the design presented in this thesis.

REFERENCES

[1] University Corporation for Atmospheric Research, "The Ionosphere," 2014. [Online]. Available: https://scied.ucar.edu/learning-zone/atmosphere/ionosphere.

[2] H. U. Frey, S. B. Mende, J. F. Arens, P. R. McCullough and G. R. Swenson, "Atmospheric Gravity Wave Signatures in the Infrared Hydroxyl OH Airglow," *Geophysical Research Letters,* vol. 27, no. 1, pp. 41-44, 2000.

[3] R. L. Davidson and G. D. Earle, "A Design Approach for Improving the Performance of Single-Grid Planar Retarding Potential Analyzers," *Physics of Plasmas,* vol. 18, no. 1, 2011.

[4] J. Westerhoff, G. Earle, R. Bishop, G. R. Swenson, S. Vadas, J. Clemmons, R. Davidson, L. Fanelli, C. Fish, V. Garg, A. Ghosh, B. B. Jagannatha, E. Kroeker, P. Marquis, D. Martin and S. Noel, "LAICE CubeSat Mission for Gravity Wave Studies," *Advances in Space Research,* vol. 56, no. 7, pp. 1413-1427, 2015.

[5] B. Ferda, "Retarding Potential Analyzer Theory and Design," Princeton University, 2015.

[6] T. Tsuda, "Characteristics of Atmospheric Gravity Waves Observed using the MU Radar and GPS Radio Occultation," *Proceedings of the Japan Academy, Series B Physical and Biological Sciences,* vol. 90, no. 1, pp. 12-27, 2014.

[7] K. Chan and W. Zhou, "Statistical Pairwise Collision Probability of the International Space Station with Debris," in *2018 Space Flight Mechanics Meeting*, Kissimmee, 2018.

[8] J. R. Wertz, D. F. Everett and J. J. Puschell, "Space Mission Engineering: The New SMAD," Hawthorn, Microcosm Press, 2015, p. 650.

[9] FreeFlyer Astrodynamics Software 7.6.0.54542, a.i. Solutions, Inc, "FreeFlyer," [Online]. Available: https://ai-solutions.com/freeflyer-astrodynamic-software/. [Accessed 28 January 2022].

[10] C. A. S. Fernandes, R. Godina, E. Rodrigues, B. A. Worke and J. P. S. Catalão, "NaS Battery Storage System Modeling and Sizing for Extending Wind Farms Performance in Crete," in *Proceedings of the 24th Australasian Universitites Power Engineering Conference*, Perth, 2014.

[11] NanoAvionics, "Products Supplied by NanoAvionics," 2020. [Online]. Available: https://nanoavionics.com/. [Accessed April 2022].

[12] Azur Space, "30% Triple Junction GaAs Solar Cell," datasheet, 2016.

[13] J. R. Wertz, D. F. Everett and J. J. Puschell, "Space Mission Engineering: The New SMAD," Hawthorne, Microcosm Astronautics Books, 2015, p. 222.

[14] Sensonor, "Ultra-High Performance Inertial Measurement Unit (IMU)," February 2020. [Online]. Available: https://satcatalog.s3.amazonaws.com/components/314/SatCatalog_-_Sensonor_AS_-_STIM300_-_Datasheet.pdf?lastmod=20210708043857. [Accessed January 2022].

[15] ANSI/AIAA American National Standard, "Mass Properties Control for Space Systems," American Institutde of Aeronautics and Astronautics, Reston, 2015.

[16] V. Larouche, "NASA Mass Growth Analysis Spacecraft & Subsystems," NASA, Hampton, 2014.

[17] Satlab, "Full-duplex Low-power S-band Transceiver," 13 August 2018. [Online]. Available: https://www.satlab.com/resources/SLDS-SRS3-1.1.pdf. [Accessed January 2022].

[18] IQ Spacecom, "S Band Antenna," September 2022. [Online]. Available: https://www.iq-spacecom.com/images/Datasheets/S_Band_Antenna_Datasheet-A4.pdf. [Accessed November 2022].

[19] NanoAvionics, "Products Supplied by NanoAvionics," 2021. [Online]. Available: https://nanoavionics.com/wp-content/uploads/2021/08/Product-Catalogue_2021-06-online-single.pdf. [Accessed January 2022].

[20] Siemens, Student Version, *NX Thermal Analysis.*